



One-pot synthesis of stable cationic gold species highly active in the CO oxidation confined into mordenite-like zeolite

T.A. Zepeda^{a,*}, A. Solís-García^a, O.E. Jaime Acuña^a, J.C. Fierro-Gonzalez^b, A. Simakov^a, V. Petranovskii^a, O. Raymond Herrera^a

^a Universidad Nacional Autónoma de México, Centro de Nanociencias y Nanotecnología, km 107 Carretera Tijuana-Ensenada, AP 14, Ensenada 22860, B.C., Mexico

^b Departamento de Ingeniería Química, Tecnológico Nacional de México en Celaya, Av. Tecnológico y Antonio García Cubas s/n. Celaya, Guanajuato 38010, Mexico

ARTICLE INFO

Keywords:

Low temperature CO oxidation
Gold catalysts
Au catalysts
Cationic gold stability
Mordenite-like zeolite
One-pot Au-zeolite synthesis

ABSTRACT

The presence of cationic gold species is a key factor for the CO oxidation over the supported gold catalysts based on non-reducible metal oxides. The deactivation of such catalysts is mainly associated with the Au nanoparticles (AuNPs) sintering and the concomitant reduction of cationic Au species. Here we report the high catalytic stability at the CO oxidation of the cationic Au species confined into a mordenite-like zeolite matrix prepared by a one-pot synthesis method. The sample with lowest Au loading (0.32 % wt.) exhibited the higher catalytic performance and stability during CO oxidation. Detailed FTIR analysis showed that the CO oxidation on sample with low Au content (0.32 wt%) occurred preferentially via CO interaction with the cationic interface Au-hydroxyl ($\text{Au}^{1+}\text{-OH}^-$) species to produce $\text{CO}_2(\text{g})$ via decarboxylation. In contrast, the sample with a high Au content (1.56 wt%) displayed lower CO oxidation ability, which was associated with a low content and less stability of cationic gold species. Proposed synthesis method permits to obtain in a one-pot way stable cationic gold species highly effectively for the CO oxidation.

1. Introduction

Rapid industrial development and the growing demand for the use of automobiles for transportation have led to an increase in use of fossil fuels, thus causing a drastic increase in atmospheric pollution [1]. Among all the atmospheric pollutants, carbon monoxide (CO) is a highly toxic gas, which causes severe human health consequences and irreversible damage to the environment [2]. The search for strategies towards decreasing atmospheric CO concentration is an urgent task, which continues attracting numerous research groups focused on improving synthesis methods and enhancement of the catalytic performance at a lower cost for this reaction [3]. One of the strategies proposed to decrease CO emissions, arising from incomplete combustion of fossil fuels in internal combustion engines, is the CO oxidation through use of catalytic converters [3].

Undoubtedly, the CO oxidation catalyzed by gold has developed into one of the most important advances in the field of catalysis, due to the extraordinary catalytic performance of supported gold in this reaction [4,5]. The role of the nature of the support used for the preparation of gold catalysts has been extensively studied [6]. The reducible supports,

such as CeO_2 , have shown to be highly efficient for the development of supported Au catalysts of the CO oxidation, due to their higher oxygen storage capacity (OSC) [6]. This property has been associated to the facile to change between reduced and oxidized states ($\text{Ce}^{3+} \leftrightarrow \text{Ce}^{4+}$), through their rapid reversible ability to oxygen uptake and release [7,8], which plays an important role in three-way catalysts. However, during reaction conditions, significant changes in the redox properties of ceria, sintering of the Au nanoparticles and low stability of cationic gold species were observed [9].

It is emphasized that alternative supports, derived from non-reducible metal oxides, have been explored in the synthesis of gold-supported catalysts [10–15]. One advantage of using non-reducible metal oxides as carriers of gold catalysts for the CO oxidation reaction is their thermal stability [16,17]. Another advantage is that these oxides frequently possess a high surface area, which facilitates improved dispersion of the gold species, consequently leading to an increased number of active sites for the reaction to take place [18,19]. In addition, non-reducible metal oxides are generally resistant to reduction and sintering, which can lead to deactivation of the catalyst [20].

Specifically, Au catalysts supported on non-reducible supports, like

* Corresponding author.

E-mail address: trino@ens.cnyn.unam.mx (T.A. Zepeda).

<https://doi.org/10.1016/j.apcatb.2023.122855>

Received 21 February 2023; Received in revised form 28 April 2023; Accepted 5 May 2023

Available online 6 May 2023

0926-3373/© 2023 Elsevier B.V. All rights reserved.

SiO₂, Al₂O₃ and zeolite, exhibit significant stability in a non-oxidizing environment [5]. Significant research has been devoted to exploring the application of gold-based catalysts supported on these specific types of materials. The findings have illustrated the viability of achieving highly efficient gold-based catalysts, supported on non-reducible materials, for catalyzing the carbon monoxide oxidation reaction.

The control of the size of the gold particles [7,10–12] and the oxidation states of the gold species [13–15], appear to be crucial for the performance of gold catalysts supported on these oxides. However, the precise mechanism involved in the activation of oxygen in this process is currently a topic of debate. Among gold species, cationic gold has demonstrated superior catalytic performance over zero-valent gold species supported on non-reducible metal oxides for CO oxidation [21]. One aspect is the involvement of cationic gold species in the process of oxygen activation, which occurs through a complex mechanism that may involve surface OH groups or water vapor desorption during CO oxidation reaction. Then, the presence of water in the reaction environment has been shown to play a crucial role in the activation of oxygen species and the promotion of catalytic activity in the presence of cationic gold species [21].

Hence, synthesizing gold-based catalysts with stable cationic gold species under reaction conditions presents a noteworthy challenge.

In recent years, the ability of zeolites to stabilize clusters and nanoparticles of foreign materials both on their surface and within their cavities has acquired particular importance [22,23]. The use of zeolites can improve the dispersion of Au clusters and nanoparticles due to the controlled pore size, their uniform morphology and high surface area values. Several studies have been reported employing a zeolite matrix as a support for Au catalysts for CO oxidation, which have emphasized ion-exchange as a method for the gold species incorporation; however, the subsequent use of calcination and thermal treatment procedures promotes the coalescence of metallic Au nanoparticles and the reduction of cationic Au species, which considerably reduces the activity of CO oxidation [13,14]. On the other hand, an interesting hypothesis was proposed, which suggests that CO can be adsorbed on cationic Au species, and, besides, could be involved in the oxygen activation, [14,15]. Therefore, there is a motivation to continue the development of novel methods to obtain highly dispersed Au catalysts, which hinder the sintering of Au clusters and the reduction of Au species. It is known that it is difficult to prepare supported nanoparticles and clusters, ultra-stable and highly dispersed, constituted by a mix of cationic and zerovalent gold species.

Zeolites are well-known regular crystalline porous dielectrics that can be used as excellent host matrices to create a wide range of unique nanocomposites by introducing guest substances as clusters inside the channels or cavities and as dispersed nanoparticles grown on their high surface area many hundreds of square meters per gram of sample [14,22,23]. The uniqueness of these matrices is given by the large volume of voids, regular in size, in their crystal structure. Especially, for mordenite-like zeolite used in this work, the accessible void volume is 12.7 % of the total crystal volume [24]. Accordingly, zeolites have a large available surface area [25]. The presence of channels and cavities with sizes ranging from 0.2 to 1 nanometer creates traps for clusters confined in them, isolating them from each other, and thus suppressing the tendency to agglomeration.

Stabilization of ions and clusters of transition metals in matrices makes it possible to stabilize unstable oxidation states and few-atom neutral and charged particles. The self-assembly of Cu, Ag and Au clusters and surface nanoparticles in mordenite has been reported [26,27]. Experimental conditions were found to be the key factors in clusters species formation in the confined space of mordenite channels favored the formation of cationic gold species.

Recently, a study was published on the immobilization of platinum metal particles encapsulated within mordenite (MOR) crystals, which exhibit extraordinary sintering resistance and excellent catalytic performance in water-gas shift reaction, CO oxidation, oxidative methane

reforming and CO₂ hydrogenation [28,29]. The result was achieved through the use of two-stage directional seed growth. These catalysts offer remarkable advantages over conventional zeolite-supported metal catalysts. Nevertheless, the proposed synthesis method is overly complex, and the synthesis requires up to 4 days [28], which significantly limits large-scale production.

Here we report new nanocomposites based on Au nanoparticles stabilized in a mordenite matrix ([Au]-MOR) synthesized using a one-pot version of the sol-gel procedure, in the absence of solvents and organic templates. Au species grow directly, and are rooted and constrained on the porous surface and inside of the mordenite matrix. To investigate the stability of Au-species during CO oxidation, *operando* infrared spectroscopy under reaction conditions was applied. Our data demonstrate the high catalytic stability of the Au¹⁺ species obtained by this method under the reaction conditions.

2. Experimental

2.1. Incorporation of Au species directly during zeolite synthesis

The synthesis of catalysts by a one-pot technique, as a variant of the sol-gel process, was performed according to the procedure described earlier [22,23,30]. To carry out the synthesis, 110 mL of a mixture of 0.1 M aqueous solutions of sodium silicate and aluminum sulfate, with a molar ratio (MR) of SiO₂/Al₂O₃ equal to 15, were prepared and stirred for 30 min. Subsequently, 10 mL or 30 mL of a 0.1 M aqueous solution of gold nitrate AuH₇N₄O₁₅ (20:10 v/v) were mixed with the former solution. The final gel with a pH value of about 9 was autoclaved at 155 °C for 48 h. Thereafter, the samples were collected at room temperature by filtration followed by washing until traces of Al, Si, Na or Au disappeared from the rinse water. The samples were likely washed multiple times until the presence of any component was no longer detected in the wash solution by ICP-AES analysis. Then, the samples were dried at room temperature for 12 h, followed by dehydration at 350 °C for 5 h. Thus, two samples were synthesized with a resulting gold loading of 0.32 and 1.56 wt%, which are labeled as [Au]-MOR-0.32 and [Au]-MOR-1.5, respectively (see Table 1).

2.2. Characterization techniques

The elemental composition of the calcined catalysts was determined by inductively coupled plasma atomic emission spectroscopy (ICP-AES) technique on a Perkin Elmer Optima 3300DV apparatus. The solid samples were first digested (in a mixture of HF, HCl, and HNO₃). The crystalline structure was studied by X-ray diffraction (XRD) on a Bruker D8 Advance instrument with Cu K α radiation, 2 θ from 10° to 70°, step size of 0.021°, and exposition time of 0.5 s. X-ray photoelectron spectra of the catalysts were recorded using a VG Escalab 200 R spectrometer equipped with a hemispherical electron analyzer and an Mg K α ($h\nu$ = 1253.6 eV) X-ray source. Before being transferred to the analytical chamber, the samples were degassed at 150 °C for 1 h. The binding energy (BE) of the C 1 s peak of the adventitious carbon at 284.5 eV was used to correct the charge effects. Analyses of the peaks were performed with a non-linear least-squares fitting method using a software provided by CASA-package. The specific surface area was determined by the BET method from the N₂-adsorption data recorded at –196 °C with an automatic Micromeritics TriStar 3000 apparatus. UV–visible spectra of the samples were recorded by the diffuse reflectance method using a Varian Cary-5000 UV–Vis spectrophotometer.

2.3. Catalytic testing for CO oxidation

The catalytic reaction system consisted of a tubular quartz micro-reactor (12.6 mm diameter) with a porous quartz frit at the middle. The reactor was connected online to a gas chromatograph Shimadzu 12-A equipped with a thermal conductivity detector. The analysis of the

Table 1

Chemical composition obtained by ICP-AES and textural properties of the catalysts.

Catalysts labeling	SiO ₂ /Al ₂ O ₃ ratio	Si/Al ratio	Na wt%	Au, wt%	Surface area (m ² g ⁻¹)		Pore volume (cm ³ g ⁻¹)		Pore Diameter (nm)
					Meso. ^a	Microp. ^b	Meso. ^c	Microp. ^d	
MOR	10.7	5.4	3.6	-	36	459	0.06	0.24	2.1
[Au]-MOR-0.32	9.0	4.5	2.4	0.32	39	438	0.08	0.21	2.0
[Au]-MOR-1.56	9.8	4.9	1.9	1.56	37	350	0.12	0.15	1.6

^a Mesoporous surface area determined using the BET equation^b Surface area of micropores was determined by the t-plot method.^c Mesopore volume at p/p₀ = 0.97.^d Micropore volume.

reactor feed and effluent was carried out using both 5 Å and Porapak Q packed columns. 100 mg of the catalyst was placed in a micro-reactor. Prior to experiments, samples were pretreated under N₂ gas flow, which was heated at a rate of 3 °C/min from room temperature up to 200 °C for an hour, then the sample was cooled down to room temperature. After the treatment stage, the N₂ flow was replaced with the reaction mixture gas (CO/O₂/N₂ molar ratio of 1/1/98) at a contact time W/F_{CO} = 30 g_{cat} h mol_{CO}⁻¹. The conversion of CO (X_{CO}) and O₂ (X_{O2}) was calculated using Eqs. 1 and 2, respectively [31].

$$X_{CO} = \frac{[CO]_{inlet} - [CO]_{out}}{[CO]_{inlet}} \quad (1)$$

$$X_{O_2} = \frac{[O_2]_{inlet} - [O_2]_{out}}{[O_2]_{inlet}} \quad (2)$$

2.4. Fourier-transform infrared (FTIR) spectroscopic investigation during the CO oxidation

2.4.1. FTIR of CO adsorbed

FTIR spectra during CO adsorption on the samples were recorded with an Agilent 660 FTIR spectrophotometer at a resolution of 4 cm⁻¹ equipped with an ISRI transmission heated-cell and in-situ high-low pressure infrared reactor with CaF₂ windows. Self-supporting wafers of the catalysts with a thickness of 60 mg cm⁻² were prepared by pressing the powdered samples at a pressure of 8 × 10³ kg cm⁻² for 20 min. The self-supporting wafers were degassed under 10⁻⁵ mbar for 1 h, before the cell was dosed with a 30 mbar pulse of CO at room temperature, and then the FTIR spectra were recorded in intervals of 10 min.

2.4.2. FTIR under reaction conditions

FTIR investigation during CO oxidation were performed on an Agilent 660 spectrophotometer using an ISRI transmission heated-cell and

in-situ high-low pressure infrared reactor with CaF₂ windows. Self-supporting wafers of the catalysts with thickness of 60 mg cm⁻² were prepared by pressing powdered samples at a pressure of 8 × 10³ kg cm⁻² for 20 min. Prior to experiments, the self-supporting wafers were flushed under N₂ gas flow, gradually increasing the temperature up to 200 °C for an hour. Then the sample was cooled down to room temperature. After the treatment stage, the flowing gas was replaced with the reaction mixture gas (CO/O₂/N₂ molar ratio of 1/1/98) at a contact time W/F_{CO} = 30 g_{cat} h mol_{CO}⁻¹. The temperature of the FTIR reactor/cell was raised from room temperature up to 200 °C at a rate of 2 °C/min. IR spectra were recorded with a resolution of 4 cm⁻¹ every 10 °C of temperature increase.

3. Results and discussion

3.1. Catalytic activity and stability

The CO conversion as a function of temperature over [Au]-MOR catalysts during CO oxidation are shown in Fig. 1a). For both samples, an increase in CO conversion was observed with the temperature rise. However, the onset of CO conversion for the [Au] MOR-0.32 sample was observed at a lower temperature compared to the [Au]-MOR-1.56 samples. The ignition temperatures for 50 % of CO conversion (T₅₀) were 45 and 77 °C for the [Au]-MOR-0.32 and [Au]-MOR-1.56 samples, respectively. The data show that the [Au]-MOR-0.32 sample was more active than the [Au]-MOR-1.56 sample, reaching the complete CO conversion at approximately 65 °C".

It is interesting to compare the results obtained for our samples, synthesized by the new method proposed in this study, with materials prepared by conventional methods. The reference sample of gold supported on commercial mordenite, reported by Tuzovskaya et al. [32], was prepared using a conventional ion exchange method with an aqueous solution of tetraammine gold(III) nitrate complex at room

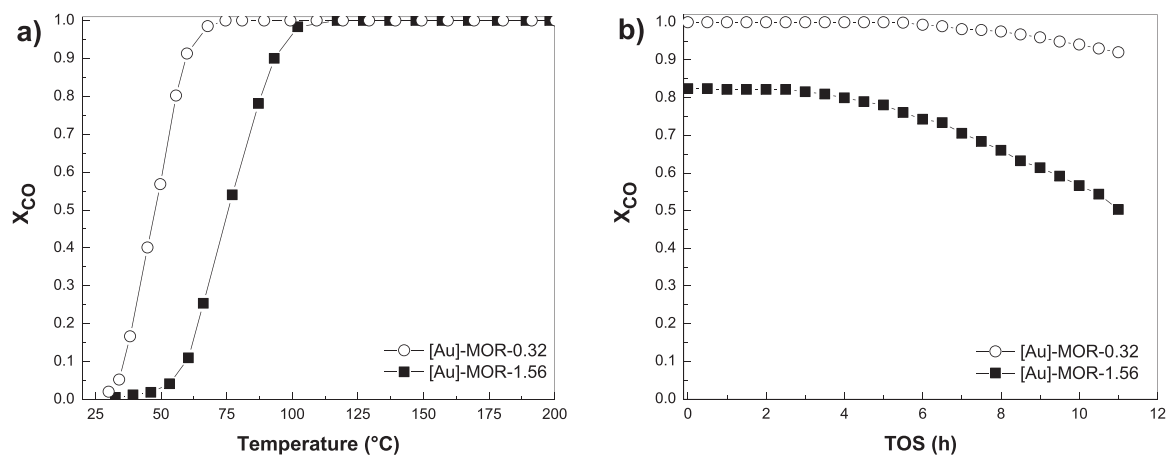


Fig. 1. a) CO conversion as a function of temperature and b) deactivation patterns during CO oxidation at 85 °C over [Au]-MOR samples using 1 % CO, 1 % O₂, N₂ balance, contact time (W/F_{CO}) of 30 g_{cat} h mol_{CO}⁻¹.

temperature, resulting in a weight loading of approximately 2.0 wt%, which was tested in the CO oxidation under experimental conditions close to those of this work. Their results showed that sample reached conversion of 50 % at 250 °C. In contrast, the synthesis method proposed in this study resulted in significantly improved catalytic properties, as evidenced by the much lower temperature required to achieve 50 % conversion in CO oxidation (65 °C for the [Au]-MOR-1.56). This suggests that the proposed method in this study has significant potential for producing materials with improved catalytic properties compared to conventional methods.

Fig. 1b) shows the performance of the [Au]-MOR samples in the CO oxidation reaction during 11 h time on stream (TOS). Again, it is observed the [Au]-MOR-0.32 sample was more active than the [Au]-MOR-1.56 sample. During the first 6 h, the [Au]-MOR-0.32 sample showed no catalytic deactivation, and then only a slight decrease of approximately 8 % in CO conversion was observed after 11 h TOS. In contrast, the CO conversion in the presence of the [Au]-MOR-1.56 sample remained stable only during the first 2 h TOS, and it then decreased rapidly. About 38 % of the initial conversion was lost on this sample after 11 h TOS. These data indicate that sample with a lower Au loading (0.32 wt%) exhibits a higher stability during the on-stream reaction compared to the [Au]-MOR-1.56 sample. It's possible that the higher stability observed in the [Au]-MOR-0.32 sample could be due to the larger number of active sites (higher cationic Au species), rather than the intrinsic stability of those sites. The observation that the [Au]-MOR-1.56 sample exhibited a loss in catalytic activity during the on-stream reaction could be related to a lower number of active sites compared to the [Au]-MOR-0.32 sample. Additionally, significant changes in the dispersion of the Au particles under reaction conditions could also contribute to the decrease in activity.

3.2. Structural characterization

The chemical composition and textural properties of a sample of sodium-mordenite (MOR) synthesized with our methodology and both [Au]-MOR catalysts are displayed in Table 1. Firstly, we note that although the initial SiO₂/Al₂O₃ ratio in the mixture of reagents for the synthesis was 15, the crystalline material formed from the prepared gel has a significantly lower value of this parameter (Table 1). However, the values of the Si/Al ratio are close to 5 as expected for MOR framework.

Fig. 2(a) shows the X-ray diffraction patterns of MOR and [Au]-MOR samples. All patterns exhibit the characteristic features of a mordenite-like zeolite structure with good crystallinity [22,23,33]. For all samples, the XRD patterns match well with the ICSD 68445 file reported for sodium-mordenite. However, there are important differences in relative

intensities of the peaks. The most noticeable are those corresponding to the planes (110), (020), and (200) in comparison with the maximum intensity of the (202) peak. Note that the crystalline planes (110), (020), and (200) intercept and contain the center point of the unit cell, while (020) and (200) intercept with the central line parallel to the [001] direction along the 12-member-ring channel and contain the center point of the unit cell. The stronger decrease in the (110), (020), and (200) intensities observed for the [Au]-MOR-0.32 sample with a smaller Au-content suggests higher incorporation of the Au-species clusters inside the channels and cavities of the zeolite framework. In contrast, for the [Au]-MOR-1.56 sample, synthesized with a higher Au-concentration, the Au nanoparticles preferentially grow on the external surface as observed from high resolution transmission electron microscopy (HRTEM) analysis (see Supplementary materials, Fig. S1). Moreover, TEM images show the growing of well dispersed nanoparticles which are well rooted and constrained on the zeolitic surface. Similar results were obtained in previous works on metal and/or semiconductor nanoparticles that grew on a mordenite matrix [22].

On the other hand, it should be noted that although the reflection peak of Au nanoparticles is absent in the [Au]-MOR-0.32 pattern, a small and broadened peak corresponding to the (111) plane of metallic Au (Au⁰) is observed at $2\theta = 38.16^\circ$ for the [Au]-MOR-1.56 sample (Fig. 2 (b)). The average size of ~ 20 nm, estimated from such a peak width using the Scherrer equation, can be taken as evidence of the presence of a bulk-like Au particles on Au]-MOR-1.56 sample, as illustrated by TEM results (Fig. 1S).

Table 1 shows that all samples have high micropore surface values. As expected, the MOR sample shows a higher value of $459 \text{ m}^2 \text{ g}^{-1}$, while for [Au]-MOR-1.56 it is significantly lower ($350 \text{ m}^2 \text{ g}^{-1}$), which correlates with a higher Au loading. For the mesopore surface, all samples exhibit similar values in the range between 36 and $39 \text{ m}^2 \text{ g}^{-1}$. Similarly, the MOR sample displays the higher micropore volume ($0.24 \text{ cm}^3 \text{ g}^{-1}$), but has a slightly lower average mesopores volume ($0.06 \text{ cm}^3 \text{ g}^{-1}$) and a larger pore diameter (2.1 nm). Thus, the lower values of surface area and pore volume corresponding to microporosity are displayed by the [Au]-MOR-1.56 sample, which could indicate that a fraction of this microporosity is blocked by gold species particles.

The pore volume values related to mesoporosity slightly increase with increasing Au content. This is associated with the blocking of micropores, leading to a noticeable increase in mesoporosity and loss of microporosity, which is confirmed by the observed decrease in the average value of the pore diameter.

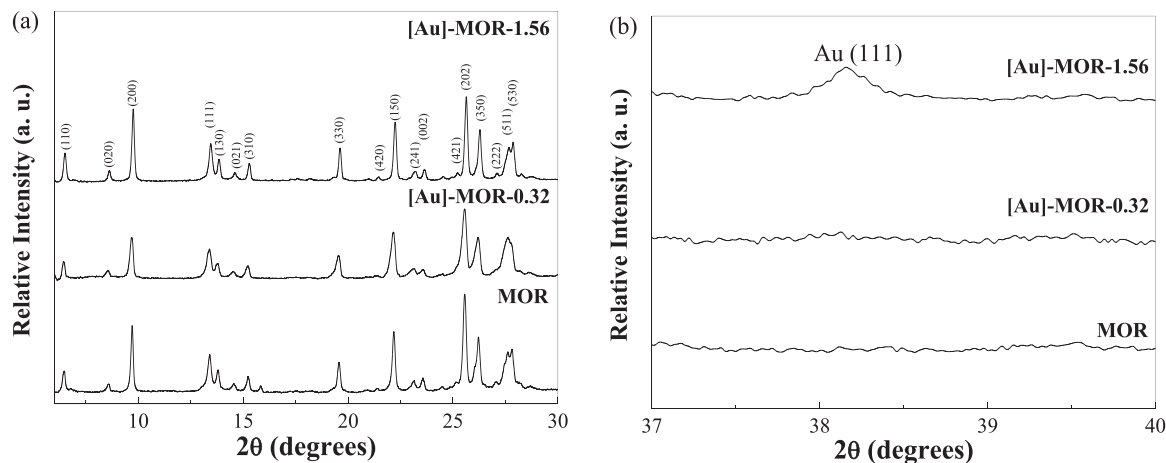


Fig. 2. a) XRD patterns for pure MOR and [Au]-MOR samples in the characteristic diffraction region of mordenite zeolite and b) region characteristic diffractions to the gold particles.

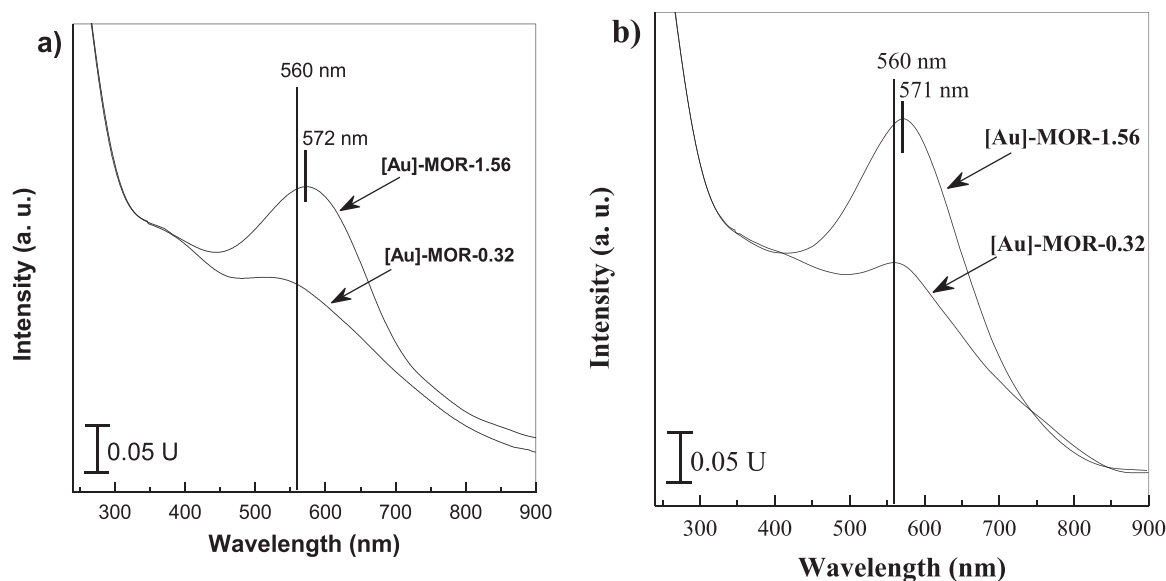


Fig. 3. DRS-UV-Vis spectra for a) freshly calcined and b) spent after reaction [Au]-MOR samples.

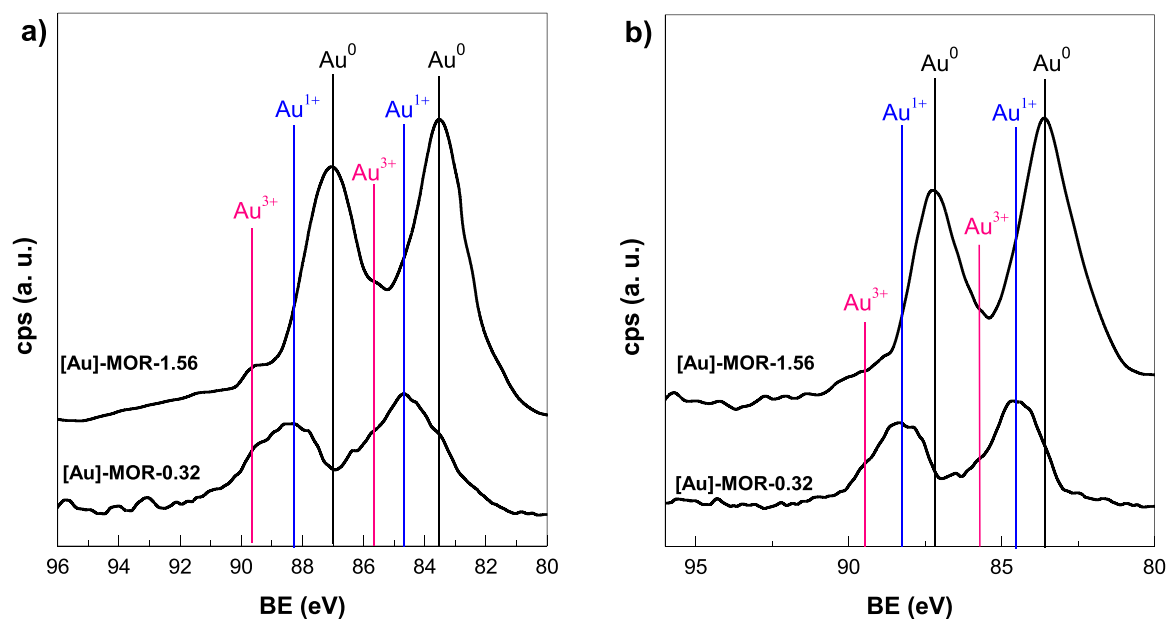


Fig. 4. XPS spectra of the Au 4f core electron levels for freshly prepared a) and spent b) [Au]-MOR samples.

Table 2

Binding energies (eV) of Au 4f core electrons, Au/Si and Au¹⁺/Au⁰ surface atomic ratios of freshly prepared and spent [Au]-MOR samples.

Sample	Au 4f _{7/2}						Au/Si at.		Au ¹⁺ /Au ⁰ at.	
	fresh			spent			fresh	spent	fresh	spent
	Au ³⁺	Au ¹⁺	Au ⁰	Au ³⁺	Au ¹⁺	Au ⁰				
[Au]-MOR-0.32	85.6 (9 %)	84.7 (68 %)	83.4 (23 %)	85.6 (7 %)	84.5 (64 %)	83.5 (29 %)	0.0025	0.0024	2.62	1.91
[Au]-MOR-1.56	85.6 (8 %)	84.7 (9 %)	83.5 (83 %)	85.6 (4 %)	84.7 (6 %)	83.6 (90 %)	0.0109	0.0091	0.11	0.06

3.3. Au species characterization

To determine the oxidation states and detect the formation of metallic particles of Au, both freshly prepared and spent samples were characterized by UV-Visible diffuse reflectance spectroscopy (UV-Vis-DRS), X-ray photoelectron spectroscopy (XPS) and high-resolution transmission electron microscopy (HRTEM).

The UV-Vis-DRS spectra corresponding to fresh [Au]-MOR samples (Fig. 3a) display a band centered around 560 nm for the [Au]-MOR-0.32 sample and around 572 nm for the [Au]-MOR-1.56 sample (Fig. 3a). In both cases, this transition could be attributed to the surface plasmon resonance (SPR) of metallic gold nanoparticles [34–36]. It arises from the collective oscillations of free electrons in the conduction band, induced by incident electromagnetic radiation with a wavelength

significantly exceeding the particle diameter.

The results indicate that the intensity, the band width, and position of the SPR band depend on the Au content (Fig. 3a). The effect of Au particles size on SPR absorption has been linked to the SPR bandwidth and intensity, which increases when the particle size increases. Indeed, it was confirmed by HRTEM (Fig. S1) and XRD results.

The UV-Vis-DRS electronic spectra of the spent [Au]-MOR samples after 11 h on stream are shown in Fig. 3b). Comparing the spectra of the samples taken before and after the reaction, one can notice that for both samples a more noticeable peak profile and an increase in the intensity of the bands at 560 and 571 nm for the SP resonance were observed for spent samples. However, the increase in the intensity of the SP resonance band is more noticeable for the [Au]-MOR-1.56 sample, containing the highest Au content. Besides, it can be noted that the full-width at half maximum of SPR band did not change for the [Au]-MOR-1.56 sample, suggesting that the size distribution of the metal particles was preserved during the reaction.

The composition and the chemical states of surface gold species were investigated by XPS. The XP spectra of the Au 4f core electron levels for freshly prepared and spent [Au]-MOR samples are shown in Fig. 4. Spectral analysis shows that, in all samples, gold exists in at least three forms: as Au⁰ (BE at 83.5 ± 0.1 eV), as Au¹⁺ (BE at 84.6 ± 0.1 eV) and as Au³⁺ (BE at 85.6 eV) [37–39].

After deconvolution of the XPS spectra of freshly prepared samples, it appears that the sample with a lower Au-content shows mainly cationic Au¹⁺ species (68 %), followed the Au⁰ fraction (23 %), while the Au³⁺ fraction is present in an insignificant proportion (9 %) (Table 2). The fraction of Au⁰ drastically increases (91 %) with increasing gold content, while the contribution of cationic Au¹⁺ and Au³⁺ species decrease considerably (9 % and 8 %, respectively). There is a higher (Au¹⁺ + Au³⁺)/Au⁰ atomic ratio for the [Au]-MOR-0.32 sample compared to the [Au]-MOR-1.56 sample (3.3 vs 0.2). Considering the total amount of gold on the surface (Au/Si at.), the [Au]-MOR-0.32 sample displayed a ratio of Au¹⁺ species 1.8 times higher with respect to its counterpart sample [Au]-MOR-1.56. From the UV-Vis-DRS and XPS results, as expected, it may conclude that the amount of metallic Au⁰ considerably increased with the Au loading.

The deconvoluted XP spectra of the spent sample with a lower Au content ([Au]-MOR-0.32) after 11 h of operation displayed three

principal BE signals at 83.5 ± 0.1, 84.6 ± 0.1 and 85.6 eV, which correspond to Au⁰, Au¹⁺ and Au³⁺ species, respectively [37–39]. In the sample with the lowest gold content ([Au]-MOR-0.32), a slight decrease of 0.1–0.2 eV in the B.E. values, corresponding to the Au⁰ and Au¹⁺ species was observed, in contrast to the [Au]-MOR-1.56 sample. This finding may indicate the presence of smaller gold particles in the [Au]-MOR-0.32 sample, which is further supported by the results of the DRS UV–vis analysis. Table 2 shows that this sample has a high fraction of cationic gold species (71 %) compared to metallic gold particles (29 %). Comparing the fraction of different Au species in the spent [Au]-MOR-0.32 sample with its counterpart before the reaction, a slight decrease in the content of cationic gold species is observed, indicating the reduction of gold, which is in agreement the UV-Vis-DRS results. In addition, there is a slight decrease in the amount of gold exposed on the surface (a decrease about 4 % of Au/Si at.). It can be noted that the Au⁵⁺/Au⁰ atomic ratio for this sample is considerably reduced in comparison with the fresh sample (3.3–2).

The sample with the highest gold content ([Au]-MOR-1.56), is predominantly composed of metallic gold (83 % and 90 % of metallic gold for the fresh and spent sample, respectively). Besides, this sample exhibits highest dispersion loss (a decrease of Au/Si at. value), about 17 %. From the UV-Vis-DRS and XPS results, we can summarize that the dispersion and stability of the cationic gold species are strongly dependent on the gold loading.

3.4. FTIR investigation during the CO oxidation reaction

The FTIR experiments under reaction conditions during CO oxidation were carried out using a gas reaction mixture CO/O₂/N₂ with molar ratio of 1/1/98, respectively and a contact time W/F_{CO} = 30 g_{cat} h mol_{CO}⁻¹. IR spectra in the ν_{CO} stretching region measured under reaction conditions at increasing temperature over [Au]-MOR-0.32 and [Au]-MOR-1.56 samples are shown in Figs. 5 and 6, respectively.

It is observed that admission of the reactive mixture led, in both cases, to the appearance of ν_{CO} bands at approximately 2112, 2125, 2165 and 2177 cm⁻¹. The bands at 2177 and 2165 cm⁻¹ could be associated to CO bonded to Al³⁺ Lewis acid sites (CO-Al³⁺) and surface hydroxyls (CO-OH), respectively [40,41], whereas those at 2125 and 2112 cm⁻¹ can be attributed to the ν_{CO} vibration mode of CO bonded to

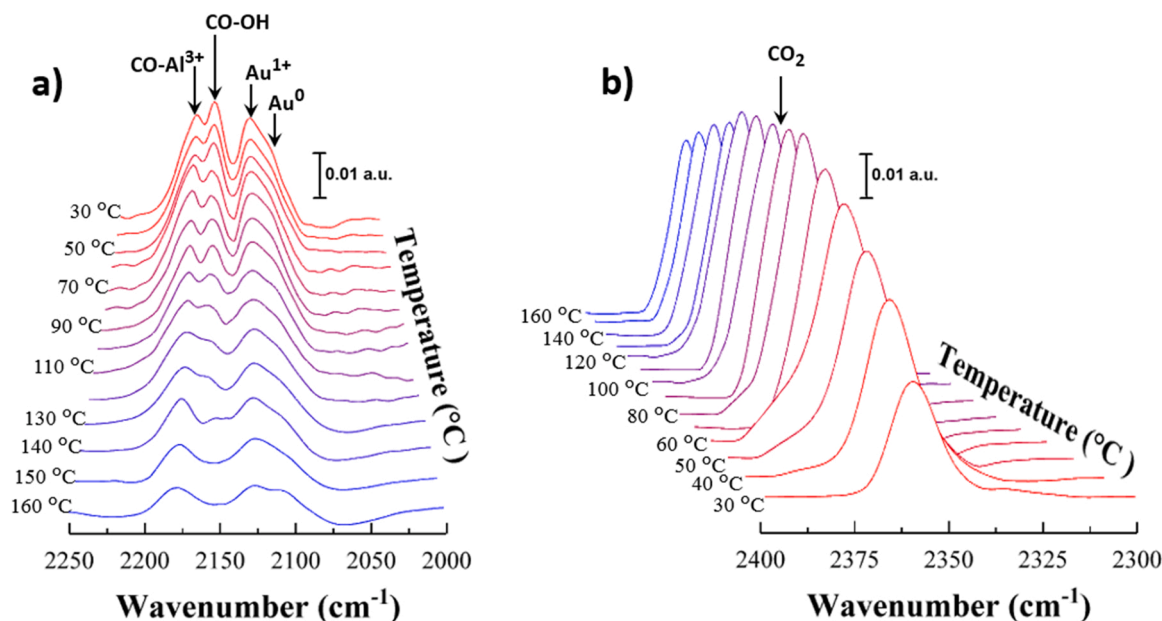


Fig. 5. Evolution of (a) ν_{CO} bands and (b) CO₂ in IR spectra for the [Au]-MOR-0.32 sample in flow of reactive mixture of CO and O₂ at increasing temperature. Total flow of 1 % CO, 1 % O₂, N₂ balance, contact time (W/F_{CO}) of 30 g_{cat} h mol_{CO}⁻¹. Prior to the measurements, the sample was treated in 60 cm³min⁻¹ of N₂ at 400 °C for 1 h.

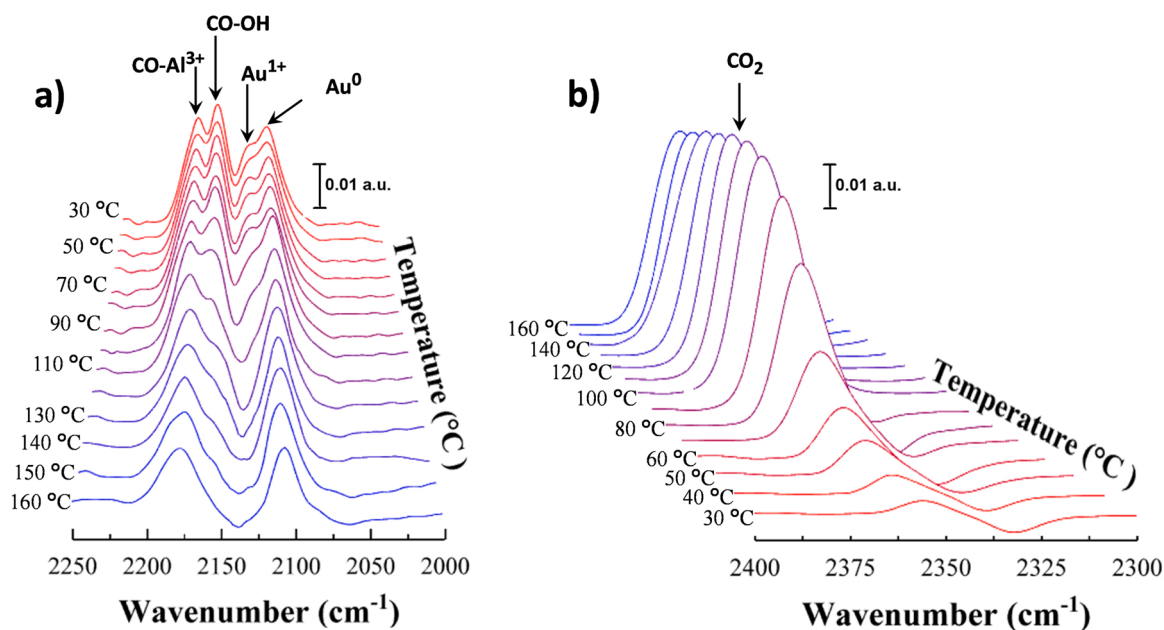


Fig. 6. Evolution of (a) ν_{CO} bands and (b) CO_2 in IR spectra of the [Au]-MOR-1.56 sample in flow of reactive mixture of CO and O_2 at increasing temperature. Total flow of 1 % CO, 1 % O_2 , N_2 balance, contact time (W/FCO) of 30 g_{cat} h molCO^{-1} . Prior to the measurements, the sample was treated in 60 $\text{cm}^3\text{min}^{-1}$ of N_2 at 400 °C for 1 h.

Au^{1+} and Au^0 sites, respectively [40,41]. All ν_{CO} bands decreased in intensity as a function of temperature. However, the 2125 cm^{-1} band, assigned to CO bonded to Au^{1+} , was still observed for the [Au]-MOR-0.32 sample even when the temperature had reached 160 °C (Fig. 5a). In contrast, the only ν_{CO} band assigned to CO bonded to Au^0 was observed at that temperature in the presence of the [Au]-MOR-1.56 sample (Fig. 6a).

The decrease in the intensities of the ν_{CO} bands was accompanied with the appearance and increase in the intensity of a band observed at 2355 cm^{-1} . FTIR signal of gas-phase CO_2 displays a doublet peak around 2335 and 2361 cm^{-1} , which correspond to the P and R branches of CO_2 (g) [42]. B.-K. Chang et al. [42] studied the mechanisms of CO oxidation over Au/TiO₂ using through FTIR spectroscopy. The authors reported

that the characteristic signs of the branches of $\text{CO}_{2(\text{g})}$ were presented over the pure TiO₂ support. The P and R branches of $\text{CO}_{2(\text{g})}$ disappeared on the Au/TiO₂ catalysts, and a new broad absorption band at 2348 cm^{-1} was observed, which was associated with adsorbed $\text{CO}_{2(\text{ad})}$ on the surface sample. However, the broadening of this band may indicate the presence of gas-phase CO_2 coupled with the adsorption of CO_2 onto the support [42]. Then, the band observed at 2355 cm^{-1} is assigned to the presence of adsorbed CO_2 species and the formation of $\text{CO}_{2(\text{g})}$ [42].

This band reached a maximum intensity at approximately 80 °C, keeping its maximum intensity until 100 °C for the [Au]-MOR-0.32 sample (Fig. 5b and S3a), and at approximately 120 °C for the [Au]-MOR-1.56 sample (Fig. 6b and S3b). The existence of a temperature

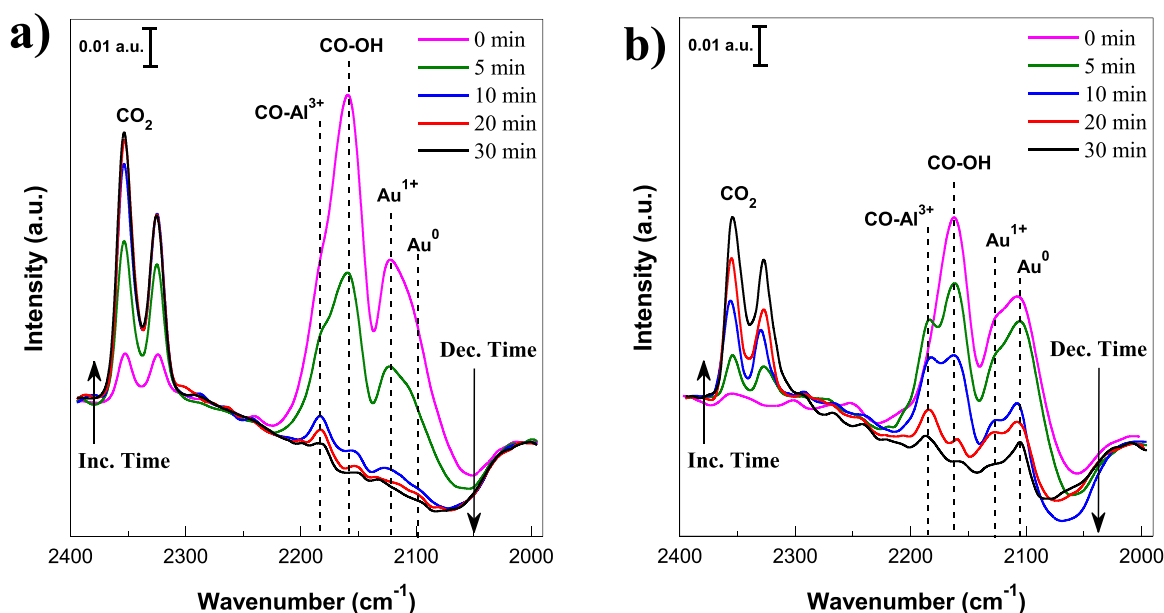


Fig. 7. IR spectra at selected times in the 2400 – 2000 cm^{-1} region recorded after pulse of 30 mbar of CO at room temperature for (a) [Au]-MOR-32 and (b) [Au]-MOR-1.56 samples. Prior to the CO pulse, the samples were treated under a N_2 flow of 60 $\text{cm}^3\text{min}^{-1}$ at 400 °C for 1 h and degassed at room temperature.

for maximum formation of $\text{CO}_{2(g)}$ (Figs. 5b and 6b), could be explained in terms of re-adsorption of CO_2 from the gas phase on the samples.

To clarify it, the FTIR spectra in the region from 1200 up to 1800 cm^{-1} they were analyzed (Fig. S4). The FTIR spectra, in this region, exhibited the signals at 1219, 1322, 1357, 1383 and 1560 cm^{-1} , characteristic of surface carbonates species [40,42–51], while the FTIR signal at 1440, 1487, 1607, 1642 and 1693 cm^{-1} , corresponds to surface bicarbonates species [40,42,44,47–54], both species bonded on the support. Along the experiment of CO oxidation, the intensities of these bands increased gradually (Fig. S5 and S6). Then, a re-adsorption of $\text{CO}_{2(g)}$ on the samples could occur, as evidenced by the formation of surface carbonaceous species during catalysis (Fig. S4).

Because all ν_{CO} bands associated with CO bonded to various gold species changed in intensity during the experiment, it is not possible to attribute the formation of CO_2 to the reactivity of a single gold carbonyl. However, it is noteworthy that the [Au]-MOR-0.32 sample, which contained more Au^{1+} , as evidenced by XPS and IR spectra under reaction conditions, was more active for CO oxidation catalysis. Therefore, it is possible to conclude that Au^+ species are more active in the CO oxidation than Au^0 ones.

In an attempt to clarify which CO-derived surface species participated in the formation of CO_2 , each sample was treated with a pulse of 30 mbar of CO at room temperature and IR spectra were measured as a function of time (Fig. 7). Prior to the experiments, the samples were heated (at a rate of 3 $^\circ\text{C}/\text{min}$) from room temperature to 200 $^\circ\text{C}$ for 1 h under 40 cm^3/min in a flowing mixture consisting of 10 % O_2 balance N_2 . Then, the samples were cooled to room temperature under the same mixture flow, and then they were degassed at 10^{-5} mbar for 30 min, followed the CO exposure. Throughout CO adsorption experiments, without oxygen supplied, CO_2 in the gas phase ($\text{CO}_{2(g)}$) was formed at room temperature, as indicated by the appearance of a band at 2355 cm^{-1} (Fig. 7) [40,41]. Interestingly, CO oxidation occurs as soon as CO was introduced into the cell with the [Au]-MOR-0.32 sample; also, on the same sample, a rapid growth of the FTIR signal for $\text{CO}_{2(g)}$ was observed (Fig. 7a).

The results show that upon admission of the CO pulse, bands characteristic of CO bonded to Al^{3+} , hydroxyl, Au^{1+} and Au^0 sites appeared in the spectra of both samples (Fig. 7). It is noticeable that the [Au]-MOR-0.32 sample contained more carbonyls on Au^{1+} than the [Au]-MOR-1.56 sample. With increasing time on stream (TOS), all ν_{CO} bands decreased in intensity. Simultaneously, bands of CO_2 appeared and increased in intensity. The formation of CO_2 even in the absence of O_2 suggests that oxygen is activated on the surface of the samples. This effect is more pronounced on the [Au]-MOR-0.32 sample. It is possible to suggest that the activation of oxygen originates from the water vapor trapped in the zeolite cavities, which occurs at the interface between the gold species and the zeolite surface. However, because all ν_{CO} bands decreased in intensity during the experiments, it is not possible to ascribe the $\text{CO}_{2(g)}$ formation to an individual gold species. It is observed that more $\text{CO}_{2(g)}$ was formed in the presence of the [Au]-MOR-0.32 sample, which contained more cationic gold. It is possible to propose that, in the absence of flowing O_2 , the activated oxygen species originate from water vapor, which might react preferentially on cationic gold. However, the involvement of zero-valence gold in the $\text{CO}_{2(g)}$ formation cannot be ruled out.

3.5. Proposed structure of gold species growth in mordenite-like zeolite

It is generally accepted that the idealized unit cell of mordenite is $\text{M}_8^+[\text{Al}_8\text{Si}_{40}\text{O}_{96}]$ with Si/Al ratio of 5, where M^+ denotes the extra-framework cations compensating the negative charge of tetrahedrally coordinated trivalent Al ions, fulfilling the condition that the sum of the charges of the cations must be equal to the number of Al atoms in the lattice. Under the conditions of our experiments, the role of such cations can be played by sodium and gold ions.

Of course, the role of Na cations in the formation of the mordenite

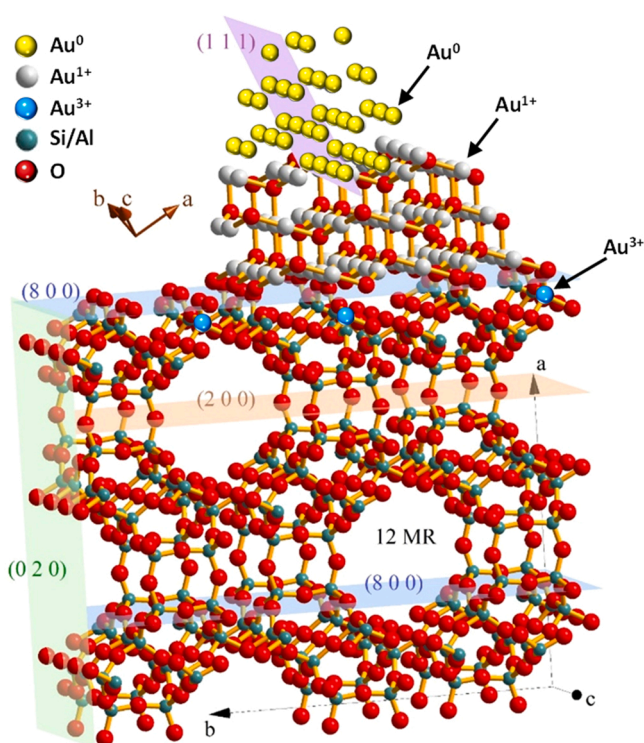
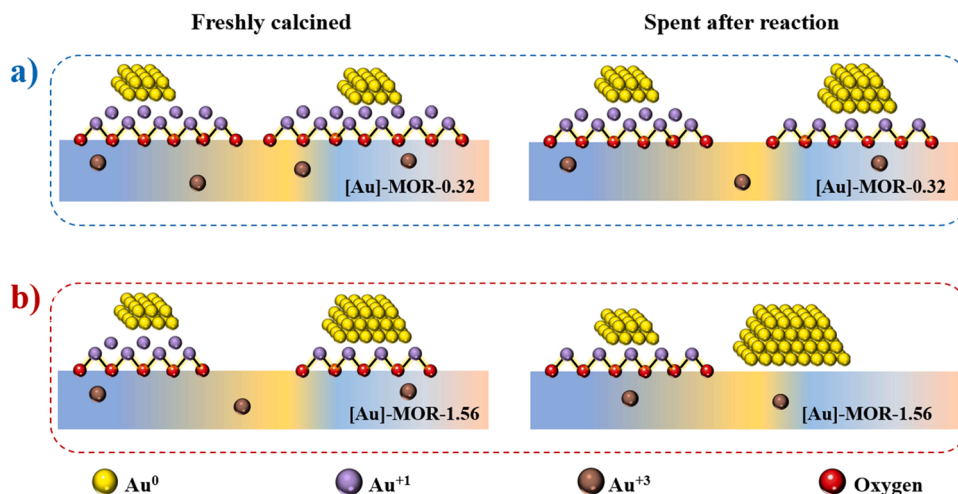


Fig. 8. Simulation of the representative Mordenite/ $\text{Au}_x\text{O}/\text{Au}$ heterostructure. The black coordinate system corresponds to mordenite, and the dark-red coordinate system corresponds to Au_2O compound. The violet (111) plane indicate the orientation of the metallic Au-cover.

structure during the synthesis is a key point [33]; sodium ions contribute both to the building unit formation and to their ordering. Nevertheless, the observed high stability of the cationic species of gold in our samples suggests that, besides clusters inside the channels, they are incorporated, predominantly, in the zeolitic matrix surface during the final stage of the crystal growing as cation Au^{1+} compensating the negative charge of the zeolite and interacting with a hydroxyl group from alumina surface, as Au^{3+} in substitution of the Al^{3+} in the framework or forming surface layers of Au_2O_3 , or as Au^{1+} constituting nanoparticles of Au_2O coupled with the surface oxygen of zeolite and covered by Au^0 or Au^{1+} species (see below).

From our results, it can be proposed, assuming that the nanoparticles on the zeolite surface grow with a structure as illustrated in a representative simulation in Fig. 8, where the Au^{3+} , Au^{1+} , and Au^0 species are present. The [Au]-MOR samples shown smaller value of the molar Si/Al ratio than pure MOR, this suggests that some fraction of gold atoms as Au^{3+} ions also could be in substitution of Al^{3+} into of MOR crystal surface. Then, the Au^{3+} species corresponds with the Al^{3+} substitution or the growth of layers with arrangement similar to the Au_2O_3 compound [55], the Au^{1+} species with the growth of the Au_2O compound nanoparticles constrained to zeolite surface, interacting with a hydroxyl group from alumina surface, and the Au^0 specie with the covering shell of metallic Au. This simulation was built employing the *Diamond* software [56] based on the XRD data reported in the ICSD #68445 for mordenite, the ICSD #44362 for metallic Au, and for Au_2O the data reported in References [57,58]. For all structures, a same scale-factor was used.

In agreement with previous studies [22,23,30], scanning electron microscopy (Fig. S2) images show that the powders samples are constituted by disk and/or spheroidal shape grains formed by packing of needle-shaped crystals which is typical for low Si/Al ratio mordenite crystals. These needle shaped crystallites grow along the [001] crystallographic direction in correspondence with the observed decreasing and



Scheme 1. Schematic representation of the gold species on the mordenite surface. a) [Au]-MOR-0.32 and b) [Au]-MOR-1.56 samples.

broadening of the first three XRD peaks with respect to those of the standard mordenite. Thus, in the last stage of growth, the final surface of mordenite crystals can be predominantly finished in different oxygen planes of framework as the (200), (020) and (800) planes, illustrated in Fig. 2, all parallel to the [001] direction along the 12-member-ring channel (12MR), which are characterized by oxygen rows parallel to [001] direction. Considering the (800) plane of the mordenite, we found that the values of the O-O distances in those oxygen rows (in this plane), as well as the distances between oxygen neighbor rows. Taking into consideration the distances of the Au-O bonds, Au-Au and O-O bonds, in the cubic arrangement of the Au_2O compound, Au_2O phase only can be grown very rooted and constrained by the oxygen surface, with preferential orientation in the [111] plane, which is perpendicular to (800) one. As can be seen in Fig. 8, such orientation of the Au_2O nanoparticle is characterized by planes of Au and O rows following the same direction of the oxygen rows of the (800) surface of mordenite. According with reference [57] in the bottom layers of the Au_2O nanoparticle the chemistry is governed by strong ionic Au-O between the surface interface and grow of species of Au over this ionic Au-O species; whereas in the up layers the chemistry could be governed by metallic Au-Au attractive interactions which reinforce the growing of a metallic Au-cover whose atoms follow the Au-rows arrangement in Au_2O . The orientation of the metallic Au-cover with $(111)_{\text{Au}}$ planes positioned as Fig. 8, it is in good agreement with those observed by HRTEM (Fig. S1). The obtained interplanar spacing value of $\sim 2.4 \text{ \AA}$ is very close to $d(111)_{\text{Au}} = 2.36 \text{ \AA}$ calculated for metallic gold from the ICSD #44362.

3.6. Catalytic activity-structure correlation

One of the main goals on the study of gold catalysts supported on non-reducible oxides for the CO oxidation reaction has been focused on understanding the role of electronic state of gold species and their participation in the mechanism for CO oxidation reaction. The cationic gold ions make an important contribution as active species in this catalysis of the CO oxidation.

Our experiments showed high performance and stability during the CO oxidation reaction of the Au-mordenite-like-zeolite framework synthesized through one-pot method. The performance and stability of the catalysts is under control of the oxidation state and sintering of Au species during the reaction. On the base of DRS UV-vis, XPS, FTIR data and the theoretical structure proposed (Fig. 8), a schematic diagram of the gold species on the mordenite surface was presented in Scheme 1. Independently of gold content, both freshly calcined samples have a similar fraction of Au^{3+} species (about 8–9 %). After 11 h on stream (Fig. 1b), the fraction of Au^{3+} species decreases 2 times for the spent

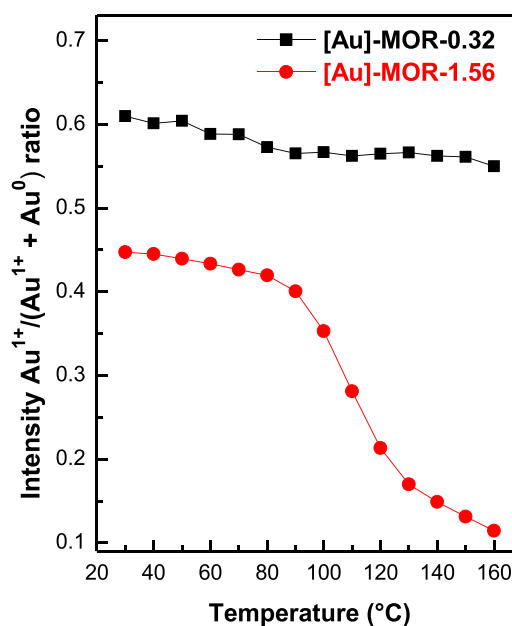


Fig. 9. Evolution of FTIR intensity bands ratio for carbonyls over different gold species $\text{Au}^{1+}/(\text{Au}^{1+} + \text{Au}^0)$ as a temperature function during CO oxidation over [Au]-MOR-0.32 and [Au]-MOR-1.56 samples. Ratio was estimated from Figs. 6–7.

[Au]-MOR-1.56 sample, while for the spent [Au]-MOR-0.32 sample a loss of the 28.5 % of this species was registered (Table 2).

The freshly calcined catalyst with a lower gold content ([Au]-MOR-0.32) is characterized by the higher amount of cationic gold species (Au^{1+} and Au^{3+}). This sample had a surface $\text{Au}^{1+}/\text{Au}^0$ atomic ratio of 3.4 times, while this ratio for the [Au]-MOR-1.56 sample was equal to 0.21. The values of this ratio, $\text{Au}^{1+}/\text{Au}^0$, decreases on the spent samples by 2.45 and 0.11 times for the [Au]-MOR-0.32 and [Au]-MOR-1.56 samples, respectively (Table 2). This is consistent with the observation from DRS UV-vis, in which a higher intensity in the plasmon resonance signal was observed for the sample with high Au content, as well as the bands associated with CO bonded to cationic and metallic gold species correlate well with the XPS results. Then, it is possible to assume that the [Au]-MOR-0.32 sample showed high reduction resistance of the cationic gold species (from XPS, besides this sample displays lower sintering of gold particles (Scheme 1a), while the [Au]-MOR-1.56 sample shows reduction of cationic gold species and sintering of Au species.

The stability of the cationic gold species can be inferred from the temperature-programmed reduction (TPR) measurements performed on the samples after the reaction. The TPR profiles for samples after 11 h of reaction, were acquiring underwent pretreatment at 200 °C under a nitrogen flow for 2 h (Fig. S9). For both samples, a hydrogen consumption peak was observed, centered at approximately 120 °C for the [Au]-MOR-1.56 sample and 126 °C for the [Au]-MOR-0.32 sample. Furthermore, in both samples, a shoulder in hydrogen consumption is noticeable around 149 °C.

The reduction peaks observed at 120–126 °C in Fig. 4 can be ascribed to the reduction of cationic gold species that have grown confined in the mordenite-type zeolite. The shoulder peak at 149 °C could be associated with the reduction of gold ions situated on the external zeolite surface, or it might be related to the reduction of Au^{3+} ions located within the interstitial sites of the zeolite.

This observation could act as a direct indicator of the cationic gold species' stability. Based on the TPR results, it can be inferred that the stability of cationic gold species is notably higher for the sample with a lower gold content, [Au]-MOR-0.32.

In the sense of evidencing the stability of the cationic gold species during the CO oxidation process the $\text{Au}^{1+}/(\text{Au}^{1+} + \text{Au}^0)$ fraction ratio was estimated via FTIR operando data from Figs. 5 and 6, as shown in the Fig. 9. From this figure, it is evident that the [Au]-MOR-0.32 sample has the higher fraction of cationic gold species. The stability of gold cations species is quite similar for both samples up to 80 °C, the $\text{Au}^{1+}/(\text{Au}^{1+} + \text{Au}^0)$ fraction ratio decreases slightly in the same manner. At temperatures above 80 °C the tendency for Au^{1+} species loss with temperature is the same for the [Au]-MOR-0.32 sample, while a drastic decrement in the fraction of such species was observed for the [Au]-MOR-1.56 sample (Fig. 9). Therefore, the higher CO oxidation performance for ([Au]-MOR-0.32 sample may be explained by the presence of higher fraction of Au^{1+} species (as mentioned above) for this sample. On the base of different gold species for both samples it is possible to expect different mechanisms for CO oxidation for these samples.

3.7. Possible reaction mechanisms for the oxidation of CO over Au species stabilized in non-reducible mordenite-like zeolite

The one-pot method employed in this work for the synthesis gold species on mordenite-like zeolite, proved that the Au^{1+} species are stabilized via bonding with surface oxygen of the zeolite framework (as well proposed in Fig. 8). This is more evident for the [Au]-MOR-0.32 sample. Thus, it can be considered that the Au^{1+} species significantly improved the catalytic performance on this sample, suggesting that the presence of these species facilitates the CO oxidation processes, as we have observed.

However, the participation of metallic gold species cannot be ruled out, as suggested by the observations on the [Au]-MOR-1.56 sample, where the possible oxidation of CO involves the perimeter Au-particle interface and the surface of gold nanoparticles as well. In this way, and taking all the data together, it is possible to consider three possible routes for the oxidation of CO over our samples, as we will discuss

below, of course each reaction route contributes to the total oxidation of CO.

3.7.1. Proposed reaction mechanism involving the participation of gold cations from the Au-zeolite interface

As has been well established that a CO molecule can be adsorbed on cationic Au^{+1} species, spilling over Au species, which could be involved in the oxygen activation, supplying oxygen for the CO oxidation reaction [59–62]. To refer to an active site model for the Au catalysts supported on no-reducible oxides that involves the participation of cationic gold species, we propose similar active site model (Scheme 2) as well reported by C.K. Costello et al. [59]. This active site involves the presence of Au cations in the perimeter Au-support interface [59,63–66]. Our results are consistent with this hypothesis, since we can assume that the gold cations ions are formed within the thin layer, probably located in the gold–zeolite interface, another possibility is that the Au^{1+} species are bonding via surface oxygen, as well proposed in the Fig. 8.

This model is based on the fact that the active site consisting of surface cationic Au^{+1} species with a hydroxyl ligand, from surface alumina hydroxyls groups, which are located with neighboring metallic Au atoms, as shown schematically represented in Scheme 2. This model is in agreement with the model of the structure proposed in Fig. 8, in which the Au^{1+} species are interacting with a hydroxyl group from alumina surface, and the Au^0 species with the covering shell of metallic Au.

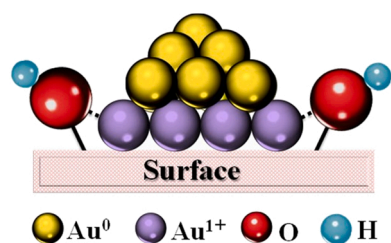
Based on the model proposed in the Scheme 2, a reaction mechanism for the catalysis of the CO oxidation, which involved the cationic gold species are proposed in Scheme 3. This model proposes that cationic Au species are located on the surface interface (Scheme 3(1)), over which it is possible to absorb the CO into an $\text{Au}^{1+}\text{-OH}^-$ bond to form a hydroxycarbonyl (Scheme 3(2)).

After this step, there are two possible reaction mechanisms proposed for the hydroxycarbonyl. The first pathway involves the decarboxylation of the hydroxycarbonyl species to produced $\text{CO}_{2(g)}$, as a consequence the formation of Au–H species occurs, (Scheme 3(3')), oxygen is subsequently absorbed, it could be dissociated on the metallic gold species (Scheme 3(4')), latter the Au–H species are oxidized anew to $\text{Au}^{1+}\text{-OH}^-$ (Scheme 3(1)).

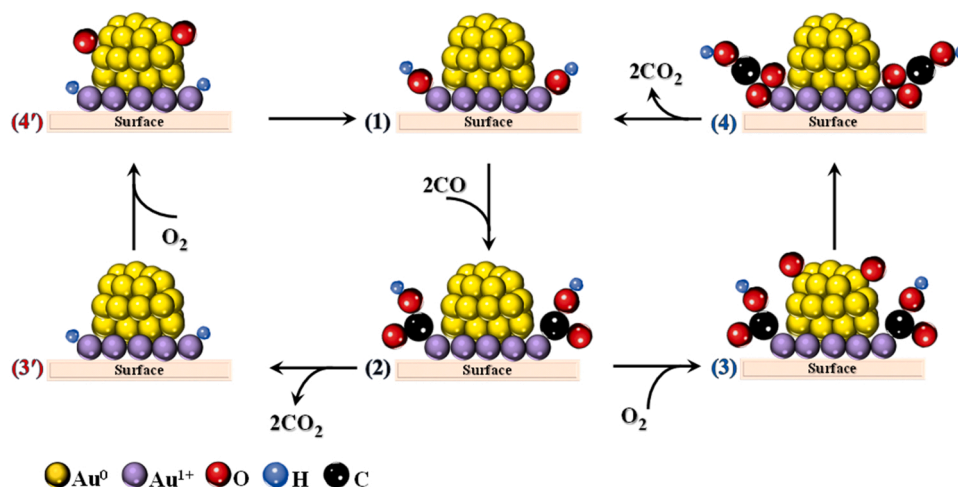
The second pathway considers that the oxygen activation could probably be on the metallic gold species (Scheme 3(3)), then the hydroxycarbonyl is oxidized to a bicarbonate, formed as an intermediary adsorbed previously to the formation of $\text{CO}_{2(g)}$ (Scheme 3(4)), which is decarboxylated to produced $\text{CO}_{2(g)}$ and Au-hydroxyl ($\text{Au}^{1+}\text{-OH}^-$), completing the reaction cycle to the initial state (Scheme 3(1)).

Undoubtedly, the role of water vapor in the oxygen activation process is a crucial step. The water vapor can have a significant impact on the catalytic activity of zeolite- and alumina-supported gold. Indeed, it is well-established that zeolites, including mordenite, have a high capacity to adsorb water in their cages. To partially avoid issues related to moisture control, we dried the samples at 200 °C under flowing N_2 for one hour, prior to the CO oxidation catalysis experiments (as described in the Experimental section). We believe that this thermal treatment helped to remove moisture and other volatile impurities that could affect the reliability of the experiments. We carried out TGA measurements on the samples after treating them with a drying process (previously mentioned). After drying the samples, a very low mass loss was observed, which leads to a lower moisture loss, compared to the fresh samples (Fig. S10). During the TGA experiments, the total moisture loss, determined once the mass loss curve was established (at 400 °C), was approximately 2.3 %. It can be noted that the onset of weight loss occurred at approximately 130 °C, suggesting that there might be little to no water loss at temperatures below 130 °C, which is the temperature at which the catalyst stability test was conducted.

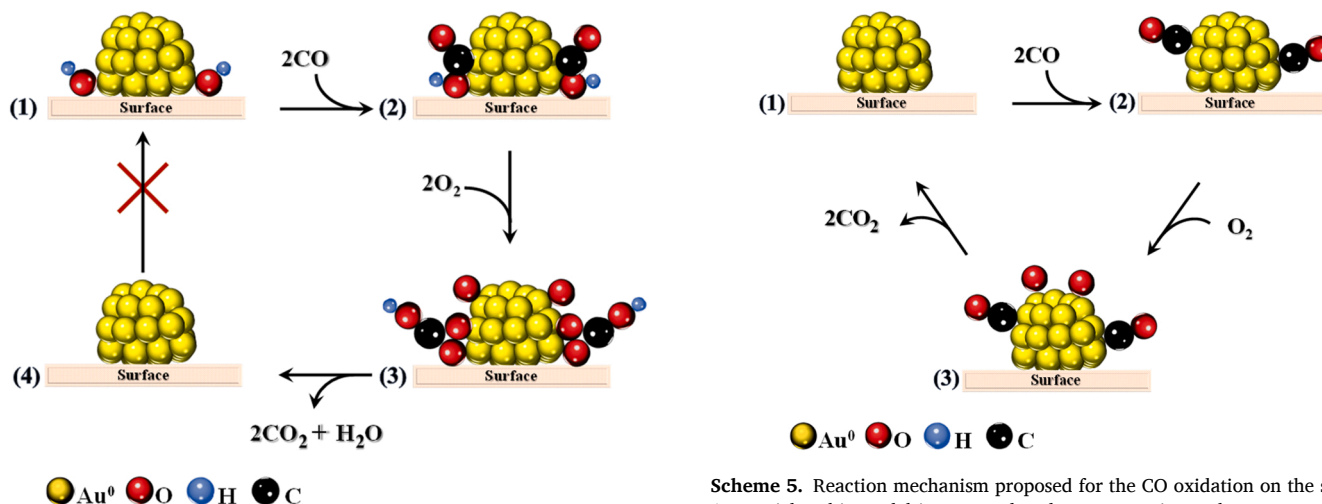
Therefore, it can be assumed that there may be some degree of control over the steam generated during the reaction process (mainly at



Scheme 2. Schematic representation of active site model for the CO oxidation over of Au catalysts supported on no-reducible oxides. Adapted from reference [59].



Scheme 3. Reaction mechanism proposed for the CO oxidation involving cationic gold species. Adapted from [59] reference. This model is proposed under our experimental resources, the oxygen activation mechanism will be omitted, but for balance and representation issues it is included.



Scheme 4. Reaction mechanism proposed for the CO oxidation that involving the catalysis in the perimeter of the Au-particle interface. This model is proposed under our experimental resources, the oxygen activation mechanism will be omitted, but for balance and representation issues it is included.

low temperatures). Nevertheless, we cannot exclude the possibility that residual water molecules within the zeolite cages might still play a role in oxygen activation and the regeneration of the peripheral hydroxyl (OH) groups associated with the gold species.

3.7.2. Proposed reaction mechanism involving the catalysis in the perimeter of Au-particle interface

To refer to an active site model for the Au catalysts supported on no-reducible oxides that involves the perimeter of the Au particles in the catalysis of the oxidation of CO. Based in ours results we proposed a mechanism for the CO oxidation that involved the cationic gold species in Scheme 4.

This model proposes that the hydroxyl groups located on the interface of Au-particles participates in the catalysis of CO oxidation via dehydroxylation of the particle interface (Scheme 4(1)). As step one, the carbon monoxide could be adsorbed on the metallic species located near of the interface particle (Scheme 4(2)), before the oxygen could be adsorbed to carry out the formation of hydroxycarbonyl species via interaction with the hydroxyl interface specie (Scheme 4(3)). Which are transformed to $\text{CO}_{2(g)}$ and $\text{H}_2\text{O}_{(g)}$, via hydroxylation, completing the

Scheme 5. Reaction mechanism proposed for the CO oxidation on the surface Au-particle. This model is proposed under our experimental resources, the oxygen activation mechanism will be omitted, but for balance and representation issues it is included.

reaction cycle (Scheme 4(4)). However, because the regeneration of the hydroxyl groups on the interface is not possible, due to the absence of cationic gold species in this model, therefore the catalytic cycle cannot be repeated (Scheme 3(4)).

3.7.3. Proposed reaction mechanism on the surface of Au-particle

It is commonly accepted that the CO oxidation over Au catalysts supported on no-reducible oxides occurs mainly on the interface of Au-particle. The most active site model is the one that involves cationic gold species at the Au-particle interface, in less participation is when the reaction occurs at the gold particle interface through surface hydroxylation.

Nevertheless, in some degree catalytic CO oxidation can occur on the surface of gold particles [67–70]. Hence, a mechanism for the CO oxidation over Au-particles is proposed as shown in Scheme 5.

In this model as a first step the CO adsorbs on the surface of Au-particle (Scheme 5(2)), subsequently the activation of oxygen could be occurred on the Au particle surfaces, preferably on the defect sites of metallic Au particle (Scheme 5(3)) [67]. Then, the CO oxidation proceeds with formation of $\text{CO}_{2(g)}$, completing the reaction cycle to the initial state (Scheme 5(1)).

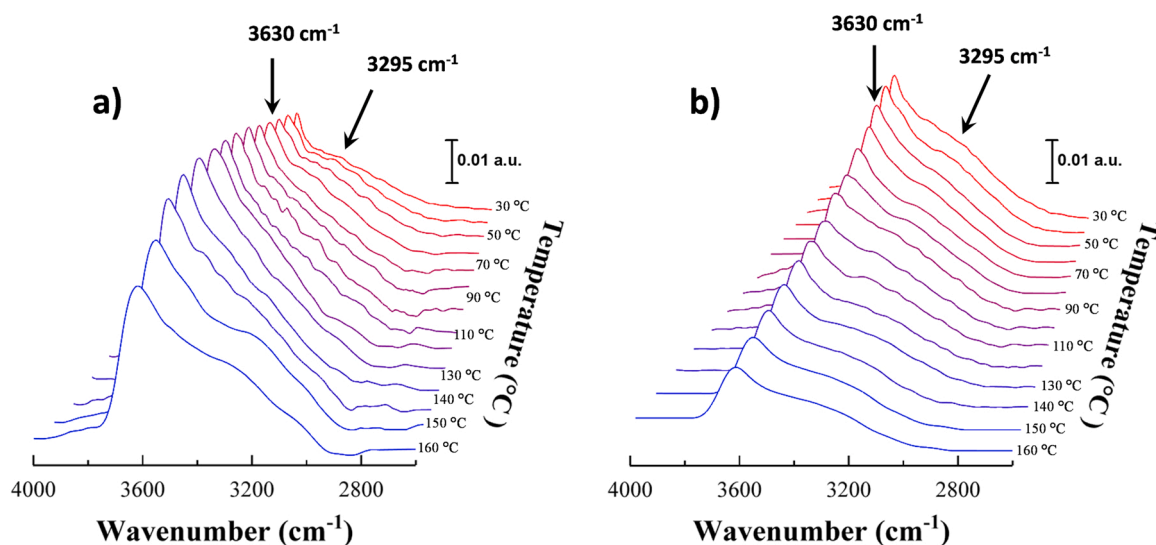


Fig. 10. FTIR spectra of the hydroxyls groups ($4000\text{--}2600\text{ cm}^{-1}$) under reaction conditions on (a) [Au]-MOR-0.32 and (b) [Au]-MOR-1.56 samples. These spectra are obtained from experiment performed in Figs. 6–7. Temperature increases back to front from 30° to 160°C with increment of 10°C . Reaction flow of 1 % CO, 1 % O_2 , N_2 balance, contact time (W/FCO) of $30\text{ g}_{\text{cat}}\text{ h molCO}^{-1}$. Before the FTIR experiments, the samples were treated under a N_2 flow of $60\text{ cm}^3/\text{min}$ at 400°C for 1 h.

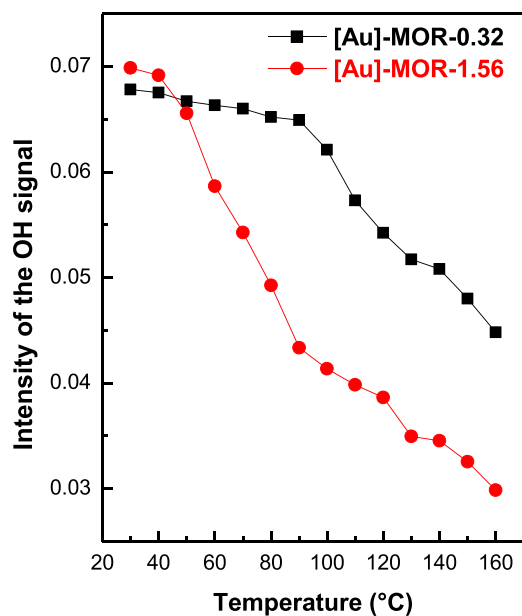


Fig. 11. Evolution of the FTIR signal of the hydroxyls groups during the oxidation of CO as temperature function. Data from Fig. 10.

3.8. Proposed mechanisms of the CO oxidation over [Au]-MOR catalysts

Considering that the gold species are supported on non-reducible oxide, the CO oxidation reaction occurs mainly at the interface of the Au-particles. Therefore, to establish which is the mechanism or mechanisms involved during the CO oxidation reaction over our samples, the role of hydroxyl groups must be considered. FTIR spectra of the region of hydroxyl groups under operando conditions as temperature function are shown in Fig. 10.

An intense signal was observed at 3630 cm^{-1} , which is characteristic to the presence of OH linked to Al ions ($-\text{Al}-\text{OH}$) [70–73]. A less intensity and broad signal is observed at 3295 cm^{-1} . This means stronger interactions of O–H bonds with the CO molecules [74,75]. Then, the CO-induced shift of this signal is to lower energy than the corresponding O–H bands, as seen confirmed by the formation of the band at 2165 cm^{-1}

(Figs. 5–6), which was assigned to CO interacting with surface hydroxyls groups (CO–OH).

It is important to clarify that prior to the reaction, the samples were dried at 400°C under N_2 flow for 1 h. Of course, we performed an experiment under the same reaction conditions, but with the absence of CO, thermal dehydroxylation before 120°C was not observed. Above 120°C a poor dehydroxylation was observed. Hence, we can assume that our observations are not caused by dehydration (drying) of the sample or thermal dehydroxylation. The evolution of the FTIR signal of the OH region during the oxidation of CO as temperature function are shown in Fig. 11. The intensity of the OH signal decrease as temperature function. Nevertheless, the behavior is quite different between the two samples.

A smaller decrease in the OH concentration was observed on the [Au]-MOR-0.32 sample among the samples studied. At the beginning of the reaction, from 30° to 90°C , a low decrease in the -OH signal as a temperature function was observed. Over this same temperature interval ($30\text{--}90^{\circ}\text{C}$), the FTIR intensity signal of carbonyl species adsorbed on Au^0 species (band at 2112 cm^{-1}) remained without significant changes as temperature function. At temperatures above of 90°C , a decrement in the intensity of this signal was observed, and their decrease was gradual as temperature function until 160°C (Fig. 5 and S7a). Whereas a gradual decrease on the intensity signal of the carbonyl species adsorbed on Au^{+1} ions (band at 2125 cm^{-1}) as a function of the increase in temperature from 30° to 160°C was observed (Fig. 5 and S7a). We must highlight that the bands corresponding to CO adsorbed on the Al^{3+} (band at 2127 cm^{-1}) and $-\text{OH}$ (band at 2165 cm^{-1}) gradually decreased over all temperature interval (Fig. S8a). These results suggest at the beginning of the reaction ($30\text{--}90^{\circ}\text{C}$), the catalysis of the oxidation of CO carried out preferentially as proposed in the reaction mechanism that involve the participation of gold cations from the interface, as represented in Scheme 3, while the metallic Au species they could be spectators. At temperatures above 90°C , our results suggested that the participation of metallic gold species has an important contribution to the total CO oxidation, developing the oxidation of CO on the surface of the gold particles, as suggested in the Scheme 5. Of course, the contribution to total CO oxidation via dehydroxylation as represented in Scheme 4, is not ruled out. However, this last possibility could be masked on the set of results. There is spectroscopic evidence of the presence of Au cations could be the principal active sites on this sample, as well inferential evidence of the presence, and particularly the participation, of hydroxyl groups in the reaction. It is unlikely that such

a mild thermal treatment can sufficiently dehydroxylate alumina, so it seems plausible that Au-hydroxyls are involved in the CO oxidation reaction. This proposal is supported considering that the fraction of cationic gold species, displayed in Fig. 9, decreased slightly during the reaction. Then, it can be assumed that in the sample with low gold content ([Au]-MOR-0.32), the catalysis of the oxidation of CO occurred preferentially via the participation of Au cationic species via CO interaction with the interface Au-hydroxyl ($\text{Au}^{1+}\text{-OH}^-$) species to produce $\text{CO}_{2(g)}$ via decarboxylation. Considering the hypothesis that the -OH groups are regenerated through the presence of cationic gold species (Scheme 3), it is therefore concluded that no significant dehydroxilation is observed during the reaction on [Au]-MOR-0.32 sample (Figs. 10 and 11).

The evolution of the -OH groups during the oxidation of CO over the [Au]-MOR-1.56 sample is shown in Fig. 11. It is possible notice a progressive dehydroxilation with the temperature increment. In the first step of the reaction ($< 90^\circ\text{C}$), a drastic decrease in the -OH signal as a temperature function was observed (Fig. 11). At the same time, the FTIR intensities of bands of CO adsorbed on Au^{1+} (at 2125 cm^{-1}) and Au^0 (at 2112 cm^{-1}) species, gradually decrease as temperature function, although in less proportion decreased the band corresponding to the CO-Au^0 species. Above of 90°C until 120°C , a drastic decrease in its intensity signal of the CO adsorbed on Au^{1+} species was observed, then continued a low decrease as a temperature function (Fig. 6 and S7b). The decrease in intensity of the CO adsorbed on Au^0 species as temperature function was more noticeable above of 90°C , from this temperature decreases gradually respect to the temperature increases. A similar behavior was observed on the band at 2165 cm^{-1} related to CO-OH species in the interval $< 90^\circ\text{C}$ (Fig. S8b). Above this temperature ($> 90^\circ\text{C}$), a drastic decrement in its intensity (CO-OH species) as temperature function was observed (Fig. 6 and S8b). The evolution of the FTIR intensity band of the CO adsorbed Al^{3+} (band at 2177 cm^{-1}) species in the temperature interval $< 90^\circ\text{C}$ was very close (Fig. S8b and S7b). This may suggest that in this temperature interval ($< 90^\circ\text{C}$), this species may have little participation or be spectators in the catalysis of the CO oxidation. At temperatures above of 90°C , the intensity of this species (CO-Al^{3+}) decreases gradually as temperature function (Fig. S8b and S7b).

As we can see, proposing the surface species involved in the catalysis of the oxidation of CO over [Au]-MOR-1.56 sample, it is quite complex. At the temperature range $< 90^\circ\text{C}$, the participation of two reaction mechanisms in the catalysis of the oxidation of CO was highlighted. The first model, probably in greater contribution, is that which involves the participation of gold cations at the interface (Scheme 3), is evidenced by the highest decrease of CO-Au^{1+} species and the decreases of the intensity signal of CO-OH species, at least in this temperature interval ($< 90^\circ\text{C}$). Simultaneously, the reaction occurs via dehydroxilation of the OH groups at the interface, as proposed in Scheme 4. This is consistent with dehydroxilation (Fig. 11) and the decrease in intensity of CO-Au^0 species (Fig. S7b), as well the evolution of the signal of CO-OH species (Fig. S8b). At temperatures above 90°C , our results suggested that the participation of metallic gold species contribute mainly to the catalysis of the CO oxidation, while the contribution of the Au^{1+} species is poor on the catalysis of the CO oxidation. The oxidation of CO on the surface of the gold particles, as suggested in the Scheme 5, is not ruled out. Their contribution in the total oxidation of CO could be masked on the combination of results.

In summary, we have offered evidence for the high stability of cationic gold species confined within mordenite-like zeolites, synthesized using a simple one-pot method without the need for solvents or organic templates. The previously proposed reaction mechanism for CO oxidation be used as an illustrative and general framework to understand the significance of gold electronic species supported on non-reducible oxides. In this model, gold cations are crucial for activating the oxygen with a hydroxyl ligand, and in together with metallic Au, they facilitate the conversion of CO to CO_2 . Additionally, this model

accounts the plausible mechanism for regenerating hydroxyl (OH) groups around the gold species.

4. Conclusions

One-pot synthesis method, in the absence of solvents and organic templates, reported in this work allowed to obtain highly stable cationic gold species confined in mordenite-like zeolite, even under CO oxidation reaction conditions. The FTIR analysis showed that the Au^{1+} species make an important contribution as active species in the catalytic CO oxidation, resulting more evident on the lowest Au content sample (0.32 % wt.), which shows a higher fraction and stability of cationic gold species. However, the oxidation of CO via dehydroxilation in the interface of the Au metallic particles contribute importantly to the CO oxidation reaction on the sample with the higher Au loading (1.56 % wt.), but it seems that temperatures above room temperature are required for the activation of this mechanism.

CRediT authorship contribution statement

Trino A. Zepeda and Juan Carlos Fierro designed the investigation, analyzed the data, and wrote the experimental section of the manuscript. Oscar Raymond Herrera, Vitalii Petranovskii and Andrey Simakoy analyzed the data, discussed the results, and participated in writing the manuscript. Alfredo Solis-Garcia conducted the experiments catalytic reactions and the FTIR measurements, analyzed the data, and participated in writing the manuscript. Oscar Jaime synthesized the samples and analyzed the data characterization.

Declaration of Competing Interest

The authors declare the following financial interests/personal relationships which may be considered as potential competing interests: Trino zepeda reports financial support was provided by National Autonomous University of Mexico Center for Nanoscience and Nanotechnology.

Data availability

Data will be made available on request.

Acknowledgements

This work was partially supported by PAPIIT-DGAPA-UNAM Grants IN112922, IT100521 and CONACYT-F003 117373 for the financial support. The authors would like to thank Francisco Ruiz, David Dominguez, Eric Flores, J. Mendoza, Israel Gradilla, and Eloisa Aparicio for technical assistance.

Appendix A. Supporting information

Supplementary data associated with this article can be found in the online version at doi:10.1016/j.apcatb.2023.122855.

References

- [1] M. Rouhani, S. Kord, Z. Mirjafary, Ga-doped phagraphene as a superior media for sensing of carbon monoxide: a detailed theoretical investigation, *Physics E* 116 (2020), 113710, <https://doi.org/10.1016/j.physe.2019.113710>.
- [2] N. Tit, K. Said, N.M. Mahmoud, S. Kouser, Z.H. Yamani, Ab-initio investigation of adsorption of CO and CO_2 molecules on graphene: role of intrinsic defects on gas sensing, *Appl. Surf. Sci.* 394 (2017) 219–230, <https://doi.org/10.1016/j.apsusc.2016.10.052>.
- [3] S. Dey, G.C. Dhal, Materials progress in the control of CO and CO_2 emission at ambient conditions: an overview, *Mater. Sci. Energy Technol.* 2 (2019) 607–623, <https://doi.org/10.1016/j.mset.2019.06.004>.
- [4] Y. Zhang, J. Zhang, B. Zhang, R. Si, B. Han, F. Hong, Y. Niu, L. Sun, L. Li, B. Qiao, K. Sun, J. Huang, M. Haruta, Boosting the catalysis of gold by O_2 activation at Au-

- SiO₂ interface, *Nat. Commun.* 11 (2020) 558, <https://doi.org/10.1038/s41467-019-14241-8>.
- [5] M. Sankar, Q. He, R.V. Engel, M.A. Sainna, A.J. Logsdail, A. Roldan, D.J. Willock, N. Agarwal, C.J. Kiely, G.J. Hutchings, Role of the support in gold-containing nanoparticles as heterogeneous catalysts, *Chem. Rev.* 120 (2020) 3890–3938, <https://doi.org/10.1021/acs.chemrev.9b00662>.
 - [6] H. Jeong, O. Kwon, B.S. Kim, J. Bae, S. Shin, H.E. Kim, J. Kim, H. Lee, Highly durable metal ensemble catalysts with full dispersion for automotive applications beyond single-atom catalysts, *Nat. Catal.* 3 (2020) 368–375, <https://doi.org/10.1038/s41929-020-0427-z>.
 - [7] Z. Zhou, S. Kooi, M. Flytzani-Stephanopoulos, H. Saltsburg, The role of the interface in CO oxidation on Au/CeO₂ multilayer nanotowers, *Adv. Funct. Mater.* 18 (2008) 2801–2807, <https://doi.org/10.1002/adfm.200800025>.
 - [8] J.L. Vincent, P.A. Crozier, Atomic level fluxional behavior and activity of CeO₂-supported Pt catalysts for CO oxidation, *Nat. Commun.* 12 (2021) 5789, <https://doi.org/10.1038/s41467-021-26047-8>.
 - [9] J.A. Hernández, S.A. Gómez, T.A. Zepeda, J.C. Fierro-González, G.A. Fuentes, Insight into the deactivation of Au/CeO₂ catalysts studied by In situ spectroscopy during the CO-PROX reaction, *ACS Catal.* 5 (2015) 4003–4012, <https://doi.org/10.1021/acscatal.5b00739>.
 - [10] Y. Zhang, B. Zhaogetu, M. Jia, C. Chen, J. Zhao, Clay-based SiO₂ as active support of gold nanoparticles for CO oxidation catalyst: pivotal role of residual Al, *Catal. Comm.* 35 (2013) 72–75, <https://doi.org/10.1016/j.catcom.2013.02.006>.
 - [11] E.V. Abkhalimov, O.A. Boeva, A.A. Odintsov, R.D. Solovov, K.N. Zhavoronkova, B. G. Ershov, The H₂-D₂ exchange reaction catalyzed by gold nanoparticles supported on γ -Al₂O₃: effect of particle size on the reaction rate, *Catal. Comm.* 133 (2020), 105840, <https://doi.org/10.1016/j.catcom.2019.105840>.
 - [12] Y.-H. Chen, C.-Y. Mou, B.-Z. Wan, Ultrasmall gold nanoparticles confined in zeolite Y: preparation and activity in CO oxidation, *Appl. Catal. B Environ.* 218 (2017) 506–514, <https://doi.org/10.1016/j.apcatb.2017.06.083>.
 - [13] J.C. Fierro-Gonzalez, B.C. Gates, Mononuclear Au^{III} and Au^I complexes bonded to zeolite NaY: catalysts for CO oxidation at 298 K, *J. Phys. Chem. B* 108 (2004) 16999–17002, <https://doi.org/10.1021/jp046171y>.
 - [14] J.M. Zamora, A.V. Boix, A. Martínez-Hernández, CO oxidation over Au supported on Mn–ZSM5 and Mn–MOR, *Catal. Comm.* 69 (2015) 212–216, <https://doi.org/10.1016/j.catcom.2015.06.018>.
 - [15] M. Haruta, S. Tsubota, T. Kobayashi, H. Kageyama, M.J. Genet, B. Delmon, Low-temperature oxidation of CO over gold supported on TiO₂, α -Fe₂O₃, and Co₃O₄, *J. Catal.* 144 (1993) 175–192, <https://doi.org/10.1006/jcat.1993.1322>.
 - [16] V. Korpelin, M.M. Melander, K. Honkala, Reducing the irreducible: dispersed metal atoms facilitate reduction of irreducible oxides, *J. Phys. Chem. C* 126 (2022) 933–945, <https://doi.org/10.1021/acs.jpcc.1c08979>.
 - [17] R. Lang, W. Xi, J.-C. Liu, Y.-T. Cui, T. Li, A.F. Lee, F. Chen, Y. Chen, L. Li, L. Li, J. Lin, S. Miao, X. Liu, A.-Q. Wang, X. Wang, J. Luo, B. Qiao, J. Li, T. Zhang, Non defect-stabilized thermally stable single-atom catalyst, *Nat. Commun.* 10 (2019) 234, <https://doi.org/10.1038/s41467-018-08136-3>.
 - [18] T. Tabakova, Recent advances in design of gold-based catalysts for H₂ clean-up reactions, *Front. Chem.* 7 (2019) 517, <https://doi.org/10.3389/fchem.2019.00517>.
 - [19] A. Goguet, C. Hardacre, I. Harvey, K. Narasimharao, Y. Saih, J. Sa, Increased dispersion of supported gold during methanol carbonylation conditions, *J. Am. Chem. Soc.* 131 (2009) 6973–6975, <https://doi.org/10.1021/ja9021705>.
 - [20] A. Jingjie Luo, A. Yanan Dong, A. Corinne Petit, B. Changhai Liang, Development of gold catalysts supported by unreducible materials: design and promotions, *Chin. J. Catal.* 42 (2021) 670–693, [https://doi.org/10.1016/S1872-2067\(20\)63743-3](https://doi.org/10.1016/S1872-2067(20)63743-3).
 - [21] X. Feng, D. Meng, Y. Yang, Z. Tan, J. Liang, C. Xiao, Au/SBA-15 catalyst prepared by ozone treatment and importance of negatively charged gold in CO oxidation by DRIFTS, *Chemosphere* 250 (2020), 126274, <https://doi.org/10.1016/j.chemosphere.2020.126274>.
 - [22] O.E. Jaime-Acuña, H. Villavicencio, J.A. Díaz-Hernandez, V. Petranovskii, M. Herrera, O. Raymond-Herrera, Atomic and electronic structure of quaternary Cd₄Zn₃S₆O₇ nanoparticles grown on mordenite, *Chem. Mater.* 26 (2016) 6152–6159, <https://doi.org/10.1021/cm5024585>.
 - [23] Oscar E. Jaime-Acuña, Humberto Villavicencio, Vitalii Petranovskii, Oscar Raymond-Herrera, Disperse orange 30 dye degradation by assisted plasmonic photocatalysis using Ag-CdZnO/zeolitic matrix nanocomposites, *Catal. Commun.* 75 (2016) 103–107, <https://doi.org/10.1016/j.catcom.2015.11.009>.
 - [24] Database of Zeolites Structures, International Zeolite Association (IZA) (<http://www.iza-structure.org/databases/>) (MOR: Framework Type (iza-structure.org)).
 - [25] Handbook of Zeolite Science and Technology, in: M.Auerbach Scott, A. Carrado Kathleen, K.Dutta Prabir (Eds.), Marcel Dekker Inc, CRC Press, New York, Basel, 2003.
 - [26] E. Smolentseva, V. Gurin, V. Petranovskii, Self-assembly of size-selected clusters and nanoparticles of Cu, Ag and Au in mordenite matrix, *Rev. Mex. Ing. Quim.* 11 (3) (2012) 469–474.
 - [27] D. Esken, S. Turner, O.L. Lebedev, G. Van Tendeloo, R.A. Fischer, Au@ZIFs: stabilization and encapsulation of cavity-size matching gold clusters inside functionalized Zeolite Imidazolate Frameworks, ZIFs, in: *Chem. Mater.*, 22, 2010, pp. 6393–6401, <http://dx.doi.org/10.1021/CM102529C>.
 - [28] D. Wang, B.C. Sheng, F.-S. Gates, Xiao, Sinter-resistant metal nanoparticle catalysts achieved by immobilization within zeolite crystals via seed-directed growth, *Nat. Catal.* 1 (2018) 540–546.
 - [29] Y.W. Chen, H.J. Chen, D.S. Lee, Au/Co₃O₄-TiO₂ catalysts for preferential oxidation of CO in H₂ stream, *J. Mol. Catal. A: Chem.* 363–364 (2012) 470–480, <https://doi.org/10.1016/j.molcata.2012.07.027>.
 - [30] Patent application MX/a/2012/013218 (Espacenet patent search database; <http://lp.espacenet.com/publicationDetails/originalDocument?CC=MX&NR=2012013218A&KC=A&FT=D&ND=4&date=20140522&DB=lp.espacenet.com&locale=es-ES> LP (accessed Oct. 3, 2014)). (<https://doi.org/10.1038/s41929-018-0098-1>).
 - [31] I.V. Chen, J.-H. Lin, J.-N. Kang, Y.-M. Yu, W.-Y. Kuo, C.-N. B.-Z. Wan, Preparation of nano-gold in zeolites for CO oxidation: effects of structures and number of ion exchange sites of zeolites, *Appl. Catal. A: Gen.* 291 (1–2) (2005) 162–169, <https://doi.org/10.1016/j.apcata.2005.02.038>.
 - [32] I.V. Tuzovskaya, A. Simakov, A.N. Pestryakov, N.E. Bogdanchikova, V.V. Gurin, M. H. Farías, H. Tiznado, M. Avalos, Co-existence of various active gold species in Au-mordenite catalyst for CO oxidation, *Catal. Comm.* 8 (7) (2007) 977–980, <https://doi.org/10.1016/j.catcom.2006.10.014>.
 - [33] Y. Suzuki, T. Wakihara, K. Itabashi, M. Ogura, T. Okubo, Cooperative effect of sodium and potassium cations on synthesis of ferrierite, *Top. Catal.* 52 (1/2) (2009) 67–74, <https://doi.org/10.1007/s11244-008-9136-6>.
 - [34] M. Ogura, Y. Kawazu, H. Takahashi, T. Okubo, Aluminosilicate species in the hydrogel phase formed during the aging process for the crystallization of FAU zeolite, *Chem. Mat.* 15 (13) (2003) 2661–2667, <https://doi.org/10.1021/cm0218209>.
 - [35] R. Tang, H. Sun, Z. Zhang, L. Liu, F. Meng, X. Zhang, W. Yang, Z. Li, Z. Zhao, R. Zeng, J. Huang, Incorporating plasmonic Au-nanoparticles into three-dimensionally ordered macroporous perovskite frameworks for efficient photocatalytic CO₂ reduction, *Chem. Eng. J.* 429 (2022), 132137, <https://doi.org/10.1016/j.cej.2021.132137>.
 - [36] S. Unal, Ion implanted Au nanoparticles in surface plasmon temperature sensing, *Mater. Lett.* 305 (2021), 130793, <https://doi.org/10.1016/j.matlet.2021.130793>.
 - [37] S.Y. Lee, H.T. Do, J.H. Kim, Microplasma-assisted synthesis of TiO₂-Au hybrid nanoparticles and their photocatalytic mechanism for degradation of methylene blue dye under ultraviolet and visible light irradiation, *Appl. Surf. Sci.* 573 (2022), 151383, <https://doi.org/10.1016/j.apsusc.2021.151383>.
 - [38] I.S. Zhidkov, E.Z. Kurmaev, S.O. Cholakh, E. Fazio, L. D'Urso, XPS study of interactions between linear carbon chains and colloidal Au nanoparticles, *Mendelev Commun.* 30 (2020) 285–287, <https://doi.org/10.1016/j.mencom.2020.05.007>.
 - [39] S. Chenakin, N. Kruse, Combining XPS and ToF-SIMS for assessing the CO oxidation activity of Au/TiO₂ catalysts, *J. Catal.* 358 (2018) 224–236, <https://doi.org/10.1016/j.jcat.2017.12.010>.
 - [40] J. Szanyi, J.H. Kwak, Dissecting the steps of CO₂ reduction: 1. The interaction of CO and CO₂ with λ -Al₂O₃: an in situ FTIR study, *Phys. Chem. Chem. Phys.* 16 (2014) 15117–15125, <https://doi.org/10.1039/C4CP00616J>.
 - [41] M.A. Centeno, K. Hadjiivanov, T.Z. Venkov, H.R. Klimek, J.A. Odriozol, Comparative study of Au/Al₂O₃ and Au/CeO₂-Al₂O₃ catalysts, *J. Mol. Catal. A: Chem.* 252 (2006) 142–149, <https://doi.org/10.1016/j.molcata.2006.02.056>.
 - [42] B.-K. Chang, B.W. Jang, S. Dai, S.H. Overbury, Transient studies of the mechanisms of CO oxidation over Au/TiO₂ using time-resolved FTIR spectroscopy and product analysis, *J. Catal.* 236 (2005) 392–400, <https://doi.org/10.1016/j.jcat.2005.10.006>.
 - [43] R.D. Shannon, Revised effective ionic radii and systematic studies of interatomic distances in halides and chalcogenides, *Acta Cryst. A* 32 (1976) 751–766, <https://doi.org/10.1107/S0567739476001551>.
 - [44] C. Morterra, A. Zecchina, S. Coluccia, A. Chiorino, I.R. Spectroscopic study of CO₂ adsorption onto γ -Al₂O₃, *J. Chem. Soc., Faraday Trans.* 73 (1977) 1544–1560, <https://doi.org/10.1039/F19777301544>.
 - [45] J.C. Lavalley, Infrared spectrometric studies of the surface basicity of metal oxides and zeolites using adsorbed probe molecules, *Catal. Today* 27 (1996) 377–401, [https://doi.org/10.1016/0920-5861\(95\)00161-1](https://doi.org/10.1016/0920-5861(95)00161-1).
 - [46] N.D. Parkyns, The influence of thermal pretreatment on the infrared spectrum of carbon dioxide adsorbed on alumina, *J. Phys. Chem.* 75 (1971) 526, <https://doi.org/10.1021/j100674a014>.
 - [47] J.B. Peri, Infrared study of adsorption of carbon dioxide, hydrogen chloride, and other molecules on “acid” sites on dry silica-alumina and γ -Alumina, *J. Phys. Chem.* 70 (1966) 410–417, <https://doi.org/10.1021/j100882a026>.
 - [48] A.M. Turek, I.E. Wachs, Acidic properties of alumina-supported metal oxide catalysts: an infrared spectroscopy study, *J. Phys. Chem.* 96 (1992) 5000–5007, <https://doi.org/10.1021/j100191a050>.
 - [49] A.C.C. Chang, S.S.C. Chuang, M. Mc, Y. Gray, Soong, In-situ infrared study of CO₂ adsorption on SBA-15 grafted with γ -(aminopropyl)triethoxysilane, *Energy Fuels* 17 (2003) 468–473, <https://doi.org/10.1021/ef020176h>.
 - [50] M.E. Potter, K.M. Cho, J.J. Lee, C.W. Jones, Role of alumina basicity in CO₂ uptake in 3-aminopropylsilyl-grafted alumina adsorbents, *Chem. Sus. Chem.* 10 (2017) 2192–2201, <https://doi.org/10.1002/cssc.201700115>.
 - [51] Z. Bacsik, R. Atluri, A.E. Garcia-Bennett, N. Hedin, Temperature-induced uptake of CO₂ and formation of carbamates in mesocaged silica modified with n-propylamines, *Langmuir* 26 (2010) 10013–10024, <https://doi.org/10.1021/la1001495>.
 - [52] A. Danon, P.C. Stair, E. Weitz, FTIR study of CO₂ adsorption on amine-grafted SBA-15: elucidation of adsorbed species, *J. Phys. Chem. C* 115 (2011) 11540–11549, <https://doi.org/10.1021/jp200914v>.
 - [53] N. Hiyoshi, K. Yogo, T. Yashima, Adsorption characteristics of carbon dioxide on organically functionalized SBA-15, *Micro Mesop. Mater.* 84 (2005) 357–365, <https://doi.org/10.1016/j.micromeso.2005.06.010>.
 - [54] A.E. Szege, A. Jaworski, N. Hedin, Chemisorption of CO₂ on diaminated silica as bicarbonates and different types of carbamate ammonium ion pairs, *Mater. Mater. Adv.* 2 (2021) 448–454, <https://doi.org/10.1039/D0MA00658K>.

- [55] Y. Odarchenko, D.J. Martin, T. Arnold, A.M. Beale, CO oxidation over supported gold nanoparticles as revealed by operando grazing incidence X-ray scattering analysis, *Faraday Discuss.* 208 (2018) 243, <https://doi.org/10.1039/c8fd00007g>.
- [56] H. Putz, K. Brandenburg, Diamond-crystal and molecular structure visualization. *Cryst. Impact. Kreuzherrenstr.* 102, 53227. Bonn, Germany. <http://www.crystallimpact.com/diamond>.
- [57] A. Filippetti, V. Fiorentini, Coexistence of ionic and metallic bonding in noble-metal oxides, *Phys. Rev. B* 72 (2005), 035128, <https://doi.org/10.1103/PhysRevB.72.035128>.
- [58] A.A. Aref, L. Xiong, N. Yan, A.M. Abdulkareem, Y. Yu, Cu₂O nanorod thin films prepared by CBD method with CTAB: substrate effect, deposition mechanism and photoelectrochemical properties, *Mater. Chem. Phys.* 127 (2011) 433–439, <https://doi.org/10.1016/j.matchemphys.2011.02.029>.
- [59] C.K. Costello, M.C. Kung, H.-S. Oh, Y. Wang, H.H. Kung, Nature of the active site for CO oxidation on highly active Au/ γ -Al₂O₃, *Appl. Catal. A: Gen.* 232 (2002) 159–168, [https://doi.org/10.1016/S0926-860X\(02\)00092-3](https://doi.org/10.1016/S0926-860X(02)00092-3).
- [60] C.K. Costello, J.H. Yang, H.Y. Law, Y. Wang, J.-N. Lin, L.D. Marks, M.C. Kung, H. H. Kung, On the potential role of hydroxyl groups in CO oxidation over Au/Al₂O₃, *Appl. Catal. A: Gen.* 243 (2003) 15–24, [https://doi.org/10.1016/S0926-860X\(02\)00533-1](https://doi.org/10.1016/S0926-860X(02)00533-1).
- [61] H.H. Kung, M.C. Kung, C.K. Costello, Supported Au catalysts for low temperature CO oxidation, *J. Catal.* (2003) 425–432, [https://doi.org/10.1016/S0021-9517\(02\)00111-2](https://doi.org/10.1016/S0021-9517(02)00111-2).
- [62] Y.-F. Han, Z. Zhong, K. Ramesh, F. Chen, L. Chen, Effects of different types of γ -Al₂O₃ on the activity of gold nanoparticles for CO oxidation at low-temperatures, *J. Phys. Chem. C* 111 (2007) 3163–3170, <https://doi.org/10.1021/jp067558z>.
- [63] N.A. Hodge, C.J. Kiely, R. Whyman, M.R.H. Siddiqui, G.J. Hutchings, Q. A. Pankhurst, F.E. Wagner, R.R. Rajaram, S.E. Golunski, Microstructural comparison of calcined and uncalcined gold/iron-oxide catalysts for low-temperature CO oxidation, *Catal. Today* 72 (2002) 133–144, [https://doi.org/10.1016/S0926-5861\(01\)00487-4](https://doi.org/10.1016/S0926-5861(01)00487-4).
- [64] S. Minico, S. Scire, C. Crisafulli, S. Gavagno, Influence of catalyst pretreatments on volatile organic compounds oxidation over gold/iron oxide, *Appl. Catal. B Environ.* 34 (2001) 277–285, [https://doi.org/10.1016/S0926-3373\(01\)00221-1](https://doi.org/10.1016/S0926-3373(01)00221-1).
- [65] M. Mavrikakis, P. Stoltze, J. Nørskov, Making gold less noble, *Catal. Lett.* 64 (2000) 101–106, <https://doi.org/10.1023/A:1019028229377>.
- [66] M. Mavrikakis, J.L. Margitfalvi, A. Fasi, M. Hegedus, F. Lonyi, S. Gobolos, N. Bogdanchikova, Au/MgO catalysts modified with ascorbic acid for low temperature CO oxidation, *Catal. Today* 72 (2002) 157–169, [https://doi.org/10.1016/S0926-5861\(01\)00489-8](https://doi.org/10.1016/S0926-5861(01)00489-8).
- [67] J. Guzman, S. Carrettin, A. Corma, Spectroscopic evidence for the supply of reactive oxygen during CO oxidation catalyzed by gold supported on nanocrystalline CeO₂, *JACS* 127 (2005) 3286–3287, <https://doi.org/10.1021/ja043752s>.
- [68] A. Corma, H. Garcia, Supported gold nanoparticles as catalysts for organic reactions, *Chem. Soc. Rev.* 37 (2008) 2096–2126, <https://doi.org/10.1039/B707314N>.
- [69] E. Smolentseva, A. Simakov, S. Beloshapkin, M. Estrada, E. Vargas, V. Sobolev, R. Kenzhin, S. Fuentes, Gold catalysts supported on nanostructured Ce–Al–O mixed oxides prepared by organic sol–gel, *Appl. Catal. B Environ.* 115–116 (2012) 117–128, <https://doi.org/10.1016/j.apcatb.2011.12.010>.
- [70] R. Kefirov, E. Ivanova, K. Hadjiivanov, S. Dzwigaj, M. Che, FTIR characterization of Fe³⁺–OH groups in Fe–H–BEA zeolite: interaction with CO and NO, *Catal. Lett.* 125 (2008) 209–214, <https://doi.org/10.1007/s10562-008-9577-3>.
- [71] A. Vimont, F. Thibault-Starzyk, J.C. Lavalley, Infrared spectroscopic study of the acidobasic properties of beta zeolite, *J. Phys. Chem. B* 104 (2000) 286–291, <https://doi.org/10.1021/jp992550t>.
- [72] A. Mihaylova, K. Hadjiivanov, S. Dzwigaj, M. Che, Remarkable effect of the preparation technique on the state of cobalt ions in BEA zeolites evidenced by FTIR spectroscopy of adsorbed CO and NO, TPR and XRD, *J. Phys. Chem. B* 104 (2006) 19530–19536, <https://doi.org/10.1021/jp0634398>.
- [73] C. Jia, P. Massiani, D. Barthomeuf, Characterization by infrared and nuclear magnetic resonance spectroscopies of calcined beta zeolite, *J. Chem. Soc. Faraday Trans. 89* (1993) 3659–3665, <https://doi.org/10.1039/FT9938903659>.
- [74] A. Zecchina, C. Otero Arean, Diatomic molecular probes for mid-IR studies of zeolites, *Chem. Soc. Rev.* 25 (1996) 187–197, <https://doi.org/10.1039/CS9962500187>.
- [75] M. Mauvezin, G. Delahay, B. Coq, S. Kieger, J.C. Jumas, J. Olivier-Fourcade, Identification of iron species in Fe–BEA: influence of the exchange level, *J. Phys. Chem. B* 105 (2001) 928–935, <https://doi.org/10.1021/jp0021906>.